J. Mech. Phys. Solids 208 (2026) 106463

Contents lists available at ScienceDirect

Journal of the Mechanics and Physics of Solids

journal homepage: www.elsevier.com/locate/jmps

Material Fingerprinting for rapid discovery of hyperelastic models: First experimental validation

Denisa Martonová [a,b], Ellen Kuhl [a,b], Moritz Flaschel [a,b,*]

[a] Institute of Applied Mechanics, Egerlandstraße 5, Friedrich-Alexander-Universität Erlangen-Nürnberg, 91058, Erlangen, Germany
[b] Department of Mechanical Engineering, 318 Campus Drive, Stanford University, California, 94305, United States

ARTICLE INFO

Keywords:
Material model discovery
Pattern recognition
Lookup table
Database
Experimental validation

ABSTRACT

Material Fingerprinting is an emerging approach for the rapid discovery of mechanical material models directly from experimental data. By interpreting a material's response in standardized experiments as its fingerprint, Material Fingerprinting employs pattern recognition to match experimental data against a precomputed database, enabling real-time model discovery. This strategy is both fast and robust, as it avoids solving potentially non-convex optimization problems. Unlike traditional calibration methods, Material Fingerprinting simultaneously selects the most suitable material model and identifies its parameters. Since the fingerprint database is fully controllable, the method guarantees interpretable and physically meaningful models. In previous work, we showed the feasibility of this concept for experiments with homogeneous or heterogeneous deformation fields using synthetically generated data. Here we present the first experimental validation of Material Fingerprinting. We carefully design a fingerprint database for uniaxial tension/compression, equibiaxial tension as well as pure and simple shear experiments. Once computed in an offline phase, this database can be reused for rapid model discovery across diverse experimental datasets. We demonstrate that this single database enables the robust and efficient discovery of hyperelastic strain energy functions to accurately characterize the isotropic mechanical responses of rubber, hydrogel, and brain tissue in less than one second on a standard personal computer. To make this approach openly accessible for rapid material model discovery across laboratories, we release the database and the implementation of Material Fingerprinting as a pip-installable Python package alongside this publication.

1. Introduction

The accurate characterization of the mechanical behavior of soft materials is fundamental for predicting their response under complex loading conditions in engineering and biomedical applications (Lemaitre and Chaboche, 1994; Avril et al., 2008; Pierron and Grédiac, 2020; Roux and Hild, 2020; Römer et al., 2025). Traditionally, this task has been addressed by calibrating parameters of phenomenological constitutive models (Hartmann, 2001; Boyce and Arruda, 2000) or, more recently, by training alternative machine learning-based models (Ghaboussi et al., 1991; Mozaffar et al., 2019; Masi et al., 2021; Klein et al., 2022; Rosenkranz et al., 2023; Fuhg et al., 2024). In both cases, the calibration process requires solving optimization problems that are often computationally expensive, susceptible to non-convexity, and prone to getting stuck in local minima. Ensuring the physical admissibility of the discovered models further complicates these optimization-based approaches (Xu et al., 2025).

* Corresponding author.
E-mail address: moritz.flaschel@fau.de (M. Flaschel).

https://doi.org/10.1016/j.jmps.2025.106463
Received 18 September 2025; Received in revised form 20 November 2025; Accepted 29 November 2025
Available online 5 December 2025

However, alternative strategies are available that bypass the need for predefined constitutive models. On one hand, model-free approaches bypass explicit constitutive equations and operate directly on experimental data instead (Kirchdoerfer and Ortiz, 2016; Ibañez et al., 2018). On the other hand, automated model discovery aims to identify interpretable constitutive equations from data using symbolic or sparse regression (Schoenauer et al., 1996; Versino et al., 2017; Guan et al., 2019; Flaschel et al., 2021; Wang et al., 2021, 2022; Linka et al., 2023; Abdusalamov et al., 2023; Martonová et al., 2024, 2025; Kissas et al., 2024; Boes et al., 2024; Abdolazizi et al., 2025; Thakolkaran et al., 2025). While these approaches reduce the reliance on predefined constitutive forms, they still rely on optimization, which may be costly or unstable in practice.

All of these approaches–whether based on calibration, machine learning, or symbolic discovery–ultimately rely on solving optimization problems, which often face challenges such as long computation times and the presence of multiple local minima due to non-convex objective functions. To address these issues, we recently proposed Material Fingerprinting (Flaschel et al., 2025b), a database-driven approach that reinterprets material characterization as a pattern recognition task. The central idea of Material Fingerprinting is that each material exhibits a unique mechanical fingerprint when tested under standardized loading conditions. The method consists of two stages: In the offline phase, Material Fingerprinting precomputes a database of fingerprints that represents a wide range of models and parameters, while in the online phase, it matches experimental data against this database to identify the best-fitting entry.

Similar database-driven strategies have proven successful in other domains: for example, magnetic resonance fingerprinting in medical imaging (Ma et al., 2013; McGivney et al., 2014), lookup-based stiffness estimation in cell mechanics (Wittwer et al., 2023), and viscoelastic model calibration in rheology (Rouze et al., 2018; Trutna et al., 2019, 2020a,b). Yet, to date, their use for mechanical model discovery remains unexplored. Material Fingerprinting differs by automatically discovering both the structure and parameters of constitutive models, without assuming a fixed functional form, and by being applicable to heterogeneous deformation fields.

This approach offers several advantages over traditional calibration strategies. Material Fingerprinting simultaneously identifies both the constitutive structure and the associated parameters, eliminating the need to assume a functional form in advance. Because the database is precomputed, model discovery does not require solving optimization problems and is therefore computationally efficient and robust. By avoiding optimization altogether, Material Fingerprinting also circumvents the problem of non-convex loss landscapes and the risk of convergence to local minima. Furthermore, the database can be fully controlled during construction, ensuring that only interpretable and physically admissible models are discovered. Finally, the concept is versatile and applicable to both homogeneous and heterogeneous experimental setups, as well as to different classes of material models.

In our earlier work, we demonstrated the feasibility of Material Fingerprinting using synthetic data for both homogeneous and heterogeneous deformation fields (Flaschel et al., 2025b). However, until now, we have not yet validated Material Fingerprinting on real experimental data. Moreover, the initial framework was limited to uniaxial tension/compression and simple shear experiments in a supervised setting.

The present study provides the first experimental validation of Material Fingerprinting. Specifically, we extend the framework in three key ways: First, we construct a more comprehensive fingerprint database that now includes not only uniaxial and simple shear tests but also pure shear and equibiaxial tension/compression, thereby broadening the range of deformation modes accessible for model discovery. Second, we design the database to be flexible, allowing for the selective inclusion of relevant subsets depending on the available experiments. Third, we propose an interpolation strategy that enables Material Fingerprinting to match the experimental data, even when the deformation states do not perfectly coincide with those precomputed in the database. In this work, we focus purely on experiments with homogeneous deformation fields, as opposed to heterogeneous tests with full-field deformation data (Grédiac, 1989; Pierron and Grédiac, 2012; Roux and Hild, 2020; Wang et al., 2021; Flaschel et al., 2021; Anton and Wessels, 2022; Wiesheier et al., 2024; Moreno-Mateos et al., 2025; Shojaee et al., 2025; Ghouli et al., 2025).

We validate the method on three canonical isotropic, incompressible hyperelastic materials: (i) rubber at different temperatures, characterized in Treloar's classical experiments (Treloar, 1944), (ii) human brain tissue, characterized for different brain regions (Budday et al., 2017), and (iii) a polymer hydrogel characterized under biaxial strain (Yohsuke et al., 2011). Rubber remains the benchmark material for hyperelastic modeling due to its well-characterized stress response over a wide range of strains and temperatures (Ogden, 1997). Brain tissue exemplifies the challenges of modeling soft biological materials, with pronounced nonlinearity, regional heterogeneity, and sensitivity to small deformations (Mihai et al., 2015a; Anssari-Benam et al., 2022). Polymer hydrogels represent a class of synthetic soft materials with high water content, bridging the gap between classical elastomers and biological tissues. Collectively, these three materials provide a diverse testbed to assess the robustness and predictive capabilities of the proposed Material Fingerprinting methodology.

By applying Material Fingerprinting in a supervised setting, we demonstrate that a single fingerprint database enables rapid, robust, and interpretable discovery of hyperelastic models that accurately reproduce the experimental responses of these distinct materials. This contribution bridges the gap between the theoretical feasibility and practical applicability of Material Fingerprinting. Beyond validating the method experimentally, we release our extended database and software as a pip-installable Python package, providing the community with an openly accessible tool for material model discovery across laboratories.

2. Material Fingerprinting

In the following, we summarize the main concepts underlying Material Fingerprinting (Flaschel et al., 2025b). Here, we extend the original framework by introducing a more comprehensive database that also includes pure shear and equibiaxial tension/compression experiments. We design this database to be used flexibly. Depending on the available experimental data, we can selectively load the relevant database subsets for Material Fingerprinting. Further, we propose an interpolation strategy to facilitate material model

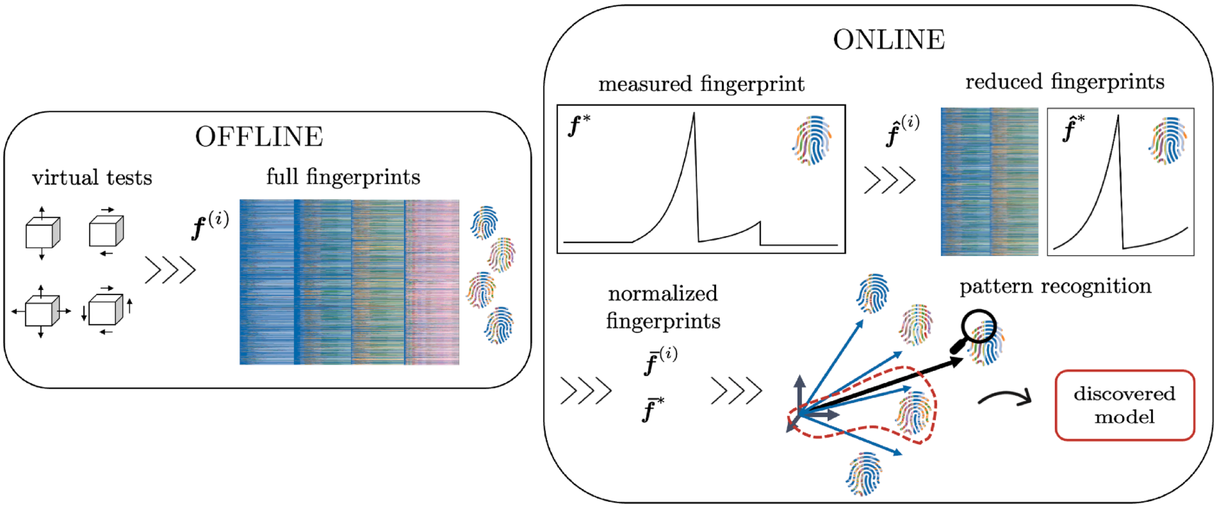

Fig. 1. Workflow for supervised Material Fingerprinting with experimental data. In the offline phase, virtual tests under different loading conditions are used to generate a database of material fingerprints. In the online phase, the experimentally measured fingerprint $\boldsymbol{f}^*$ as well as the database of full fingerprints $\boldsymbol{f}^{(i)}$ are processed into reduced and normalized fingerprints, $\bar{\boldsymbol{f}}^*$ and $\bar{\boldsymbol{f}}^{(i)}$, and the measurement is compared against the precomputed database using pattern recognition. This enables the identification of the closest matching fingerprint and thereby the rapid discovery of the underlying material model and its parameters.

discovery with Material Fingerprinting for cases when the experimental data provide deformation levels that differ from those in the database. Fig. 1 provides a schematic workflow for supervised Material Fingerprinting for experimental data as described in detail in the following subsections.

2.1. Database

In an offline phase, we generate a general database for experiments with homogeneous deformation fields at large deformations that we will then use for Material Fingerprinting on all experimental datasets considered in this work. We focus on incompressible hyperelasticity, such that the material models are defined through the strain energy density function

$$W(\boldsymbol{F};\boldsymbol{\theta},\boldsymbol{\alpha}) = \tilde{W}(\boldsymbol{F};\boldsymbol{\theta},\boldsymbol{\alpha}) - p[J-1], \tag{1}$$

where $\boldsymbol{F}$ is the deformation gradient with determinant $J = \det(\boldsymbol{F})$, and p is a Lagrange multiplier enforcing the incompressibility constraint $J = 1$. We note that, in the fully incompressible limit $J = 1$ considered throughout the work, the volumetric term $p[J-1]$ does not contribute to the strain energy density in Eq. (1), but it remains essential to recover the correct stress components. The vectors $\boldsymbol{\theta}$ and $\boldsymbol{\alpha}$ contain material parameters. We distinguish between homogeneity parameters $\boldsymbol{\theta}$, which fulfill the property

$$\tilde{W}(\boldsymbol{F};a\,\boldsymbol{\theta},\boldsymbol{\alpha}) = a\,\tilde{W}(\boldsymbol{F};\boldsymbol{\theta},\boldsymbol{\alpha}), \quad \forall a \in \mathbb{R}, \tag{2}$$

and non-homogeneity parameters $\boldsymbol{\alpha}$ that do not fulfill this property in general. The first Piola stress, or nominal stress, follows from the strain energy density function through differentiation

$$\boldsymbol{P}(\boldsymbol{F};\boldsymbol{\theta},\boldsymbol{\alpha}) = \frac{\partial W(\boldsymbol{F};\boldsymbol{\theta},\boldsymbol{\alpha})}{\partial \boldsymbol{F}}. \tag{3}$$

For the load cases considered in this work, we compute the Lagrange multiplier p by considering the constraint $P_{33} = 0$, see Appendix A. The Lagrange multiplier scales linearly with the homogeneity parameters $\boldsymbol{\theta}$, $p(\boldsymbol{F};a\,\boldsymbol{\theta},\boldsymbol{\alpha}) = a\;p(\boldsymbol{F};\boldsymbol{\theta},\boldsymbol{\alpha})$, and due to the linearity of the differentiation operator, we notice that this condition generalizes to the entire first Piola stress

$$\boldsymbol{P}(\boldsymbol{F};a\,\boldsymbol{\theta},\boldsymbol{\alpha}) = a\;\boldsymbol{P}(\boldsymbol{F};\boldsymbol{\theta},\boldsymbol{\alpha}), \quad \forall a \in \mathbb{R}. \tag{4}$$

For generating the database, we follow our initial work (Flaschel et al., 2025b) and consider the isotropic incompressible Blatz-Ko (Blatz and Ko, 1962), Demiray (Demiray, 1972), Gent (Gent and Thomas, 1958), Holzapfel-type (Holzapfel et al., 2004), Mooney-Rivlin (Rivlin, 1950), Neo-Hooke (Treloar, 1944), and Ogden (Ogden, 1972) models. Table 1 details the strain energy densities and the chosen parameter ranges for generating the fingerprints for each model.

For each material model and each parameter instantiation, we generate the materials' fingerprints considering uniaxial tension/-compression (UT), simple shear (SS), pure shear (PS), and equibiaxial tension/compression (ET) experiments. In particular, by as-

Table 1
Material models considered during database generation in the supervised setting.

Models	Strain energy density W	Parameters ranges	# Fingerprints
Blatz-Ko	$\theta_1[I_2-3]-p[J-1]$	$\theta_1=1.0$	1
Demiray	$\theta_2[\exp(\alpha_2[I_1-3])-1]-p[J-1]$	$\theta_2=1.0, \alpha_2\in[0.1,50.0]$	500
Gent	$-\theta_3\ln(1-\alpha_3[I_1-3])-p[J-1]$	$\theta_3=1.0, \alpha_3\in[0.1,50.0]$	500
Holzapfel-type	$\theta_4[\exp\left(\alpha_4[I_1-3]^2\right)-1]-p[J-1]$	$\theta_4=1.0, \alpha_4\in[0.1,50.0]$	500
Mooney-Rivlin	$\theta_5[I_1-3]+\theta_1[I_2-3]-p[J-1]$	$\theta_5\in[0.1,50.0], \theta_1=1.0$	500
Neo-Hooke	$\theta_5[I_1-3]-p[J-1]$	$\theta_5=1.0$	1
Ogden	$\theta_6[\lambda_1^{\alpha_6}+\lambda_2^{\alpha_6}+\lambda_3^{\alpha_6}-3]-p[J-1]$[1]	$\theta_6=1.0, \alpha_6\in[-25.0,25.0]$	500
			$n_d=2502$

[1]The positive parameter θ_6 replaces the classical leading Ogden parameter μ/α_6. The shear modulus can be computed through $\mu=\theta_6\,\alpha_6$.

suming material incompressibility, we consider four deformation modes characterized by the following deformation gradients

$$
\begin{aligned}
\boldsymbol{F}_{\mathrm{UT}} &= \mathrm{diag}\,\{\,\lambda_{\mathrm{UT}}, 1/\sqrt{\lambda_{\mathrm{UT}}}, 1/\sqrt{\lambda_{\mathrm{UT}}}\,\},\\
\boldsymbol{F}_{\mathrm{SS}} &= \mathrm{diag}\,\{\,1,1,1\,\}+\gamma_{\mathrm{SS}}\,\boldsymbol{e}_1\otimes\boldsymbol{e}_2,\\
\boldsymbol{F}_{\mathrm{PS}} &= \mathrm{diag}\,\{\,\lambda_{\mathrm{PS}}, 1, 1/\lambda_{\mathrm{PS}}\,\},\\
\boldsymbol{F}_{\mathrm{ET}} &= \mathrm{diag}\,\{\,\lambda_{\mathrm{ET}}, \lambda_{\mathrm{ET}}, 1/\lambda_{\mathrm{ET}}^2\,\},
\end{aligned}
\tag{5}
$$

where the term $\gamma_{\mathrm{SS}}\,\boldsymbol{e}_1\otimes\boldsymbol{e}_2$ indicates shear in the $\boldsymbol{e}_1\boldsymbol{e}_2$-plane in the $\boldsymbol{e}_1$ direction. We evaluate these deformation modes at $n_{\mathrm{UT}}=n_{\mathrm{PS}}=n_{\mathrm{ET}}=1000$ equidistant stretch levels $\lambda_{\mathrm{UT}},\ \lambda_{\mathrm{PS}},\ \lambda_{\mathrm{ET}}$ between 0.1 and 10, respectively, and at $n_{\mathrm{SS}}=1000$ equidistant shear strain levels γ_{SS} between 0 and 10. We intentionally chose these stretch and strain ranges to exceed the ranges of common physical experiments to build a database that generalizes Material Fingerprinting to various experimental datasets. For each material model and each parameter instantiation, we compute the first Piola stress component P_{11} for uniaxial tension/compression, pure shear, and equibiaxial tension/compression, and the shear stress component P_{12} for simple shear across all stretches and shear strain ranges; see Appendix A for a detailed description of the stress computations for all deformation modes and all considered material models. The computed stress components are then concatenated in the fingerprint vectors $\boldsymbol{f}^{(i)}\in\mathbb{R}^{n_f}$ with $n_f=n_{\mathrm{UT}}+n_{\mathrm{SS}}+n_{\mathrm{PS}}+n_{\mathrm{ET}}$ and $i=1,\ldots,n_d$, where n_d is the total number of generated fingerprints as exemplified in Table 1. We store all n_d fingerprints alongside the corresponding material model information in the database. Importantly, we only need to generate this database once; from now on, it can be repeatedly used for rapid material model discovery with Material Fingerprinting.

Some of the models considered during the database generation result in nonphysical stress responses under extreme deformations. Specifically, the Gent model exhibits a singularity from a zero in its denominator, and the Demiray and Holzapfel-type models result in unrealistically high stress values because of their exponential nature. Despite these unrealistic responses, we keep the fingerprints of these models in the database, as these models might be preferred choices for materials that are subjected to small or moderate strains, such as, for example, tissues in biomedical applications. As we show in the subsequent section, our algorithm is designed such that only those entries of the fingerprints that fall within the stretch/strain range of the experimental data are eventually considered.

The computation of each fingerprint depends on the chosen material model and its parameters, that is, $\boldsymbol{f}^{(i)}(\boldsymbol{\theta},\boldsymbol{\alpha})$. Because the fingerprints contain only stress measurements that fulfill the homogeneity property in Eq. (4), $\boldsymbol{f}^{(i)}(a\,\boldsymbol{\theta},\boldsymbol{\alpha})=a\,\boldsymbol{f}^{(i)}(\boldsymbol{\theta},\boldsymbol{\alpha})$. Scaling the homogeneity parameters only changes the magnitude of the fingerprint vector while its direction remains unchanged. Therefore, storing a single fingerprint for parameters $\boldsymbol{\theta}$ and $\boldsymbol{\alpha}$ in the database makes it unnecessary to generate additional fingerprints for scaled parameters $a\,\boldsymbol{\theta}$ and $\boldsymbol{\alpha}$. As we demonstrate in Section 2.2, once a material model has been discovered by the pattern recognition algorithm, the scaling parameter a, which determines the correct magnitude of the parameter vector $\boldsymbol{\theta}$, can be computed directly.

In contrast to our original strategy, in which we stored normalized fingerprints in the database that could be directly used for pattern recognition (Flaschel et al., 2025b), we now store fingerprints that are not normalized. We shift the fingerprint normalization to the online phase, during which we know the precise experimental ranges of stretches/strains. In this way, the database can be used for Material Fingerprinting, even if the experimental data is provided at different deformation states than those considered during the database generation, as we describe in Section 2.2.

2.2. Pattern recognition

In this section, we focus on the pattern recognition step at the core of Material Fingerprinting, which we employ in the online phase to discover a material model from the available experimental data using the precomputed database of fingerprints. Since the deformation states applied during the experiments may differ from those represented in the database, a preprocessing step is required before the actual pattern recognition can take place. This preprocessing aligns the experimental data with the fingerprint database by matching their deformation states. The experimentally measured data may include uniaxial tension/compression, simple shear, pure shear, or biaxial tension/compression data – or arbitrary combinations of these – at imposed stretch/strain levels $\lambda_{\mathrm{UT}},\ \gamma_{\mathrm{SS}},\ \lambda_{\mathrm{PS}},\ \lambda_{\mathrm{ET}}$. To enable comparison, we use linear interpolation to approximate the experimental stresses at the stretch/strain levels represented

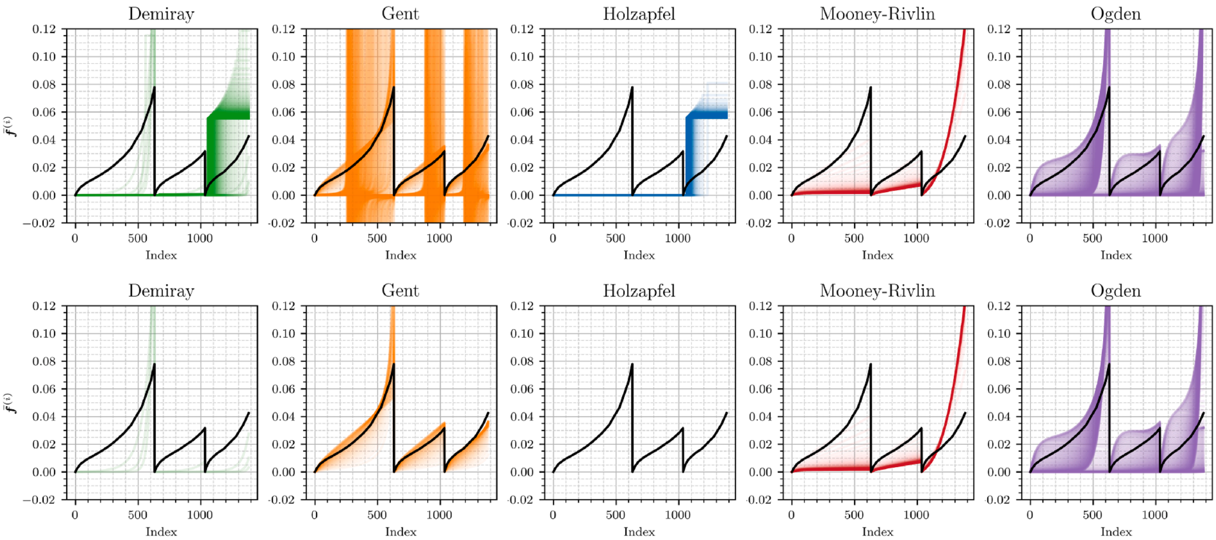

Fig. 2. Illustration of the pattern recognition algorithm at the core of Material Fingerprinting using uniaxial tension, equibiaxial tension, and pure shear tests of rubber at 20 °C. The measurement $\bar{\boldsymbol{f}}^*$, illustrated by a black curve, is compared to all entries in the database, illustrated by colored regions. The database entries are grouped and visualized separately for each model, excluding simple models that have a single parameter only. The top row illustrates all fingerprints in the database. The bottom row shows only those fingerprints that are physically reasonable for the stretch/strain range of the experiment, that is, excluding curves with singularities and unrealistically large stress values. As the considered experimental data contains stretches up to $\lambda_{\mathrm{UT}} \approx 7$, the exponential Demiray and Holzapfel-type models in our database exhibit unrealistically large stress responses.

in the fingerprint database. If a stretch/strain level in the database lies beyond the experimental range, we set the corresponding stress value to zero. This procedure yields a measured fingerprint vector $\boldsymbol{f}^* \in \mathbb{R}^{n_f}$, which is sparse wherever no experimental data are available.

We then compare the measured fingerprint $\boldsymbol{f}^* \in \mathbb{R}^{n_f}$ with the fingerprint database to discover the best-matching material model. To this end, we construct the reduced fingerprint vectors $\hat{\boldsymbol{f}}^{(i)}$, $\hat{\boldsymbol{f}}^* \in \mathbb{R}^{\hat{n}_f}$, with $\hat{n}_f \leq n_f$, which contain only those entries of $\boldsymbol{f}^{(i)}$ and $\boldsymbol{f}^*$ for which experimental data are available – that is, where $\boldsymbol{f}^*$ is nonzero. Then, we normalize the reduced fingerprint vectors and the corresponding homogeneity parameters in the database

$$\bar{\boldsymbol{f}}^{(i)} = \frac{\hat{\boldsymbol{f}}^{(i)}}{\|\hat{\boldsymbol{f}}^{(i)}\|}, \ \bar{\boldsymbol{\theta}}^{(i)} = \frac{\boldsymbol{\theta}^{(i)}}{\|\hat{\boldsymbol{f}}^{(i)}\|}, \ \bar{\boldsymbol{f}}^* = \frac{\hat{\boldsymbol{f}}^*}{\|\hat{\boldsymbol{f}}^*\|}. \tag{6}$$

Finally, we determine the closest fingerprint in the database by evaluating the inner product of the measured fingerprint with each entry in the database and selecting the one with the largest inner product

$$i^* = \underset{i=1,\dots,n_d}{\arg\max} \ \bar{\boldsymbol{f}}^{(i)} \cdot \bar{\boldsymbol{f}}^*. \tag{7}$$

As the inner product of the fingerprints $\bar{\boldsymbol{f}}^{(i)}$ and $\bar{\boldsymbol{f}}^*$ is related to the cosine of the angle $\beta^{(i)}$ between the fingerprint vectors, it is also denoted as cosine similarity $\mathrm{cs}^{(i)}$

$$\mathrm{cs}^{(i)} = \cos\left(\beta^{(i)}\right) = \frac{\bar{\boldsymbol{f}}^{(i)} \cdot \bar{\boldsymbol{f}}^*}{\|\bar{\boldsymbol{f}}^{(i)}\| \, \|\bar{\boldsymbol{f}}^*\|} = \bar{\boldsymbol{f}}^{(i)} \cdot \bar{\boldsymbol{f}}^*. \tag{8}$$

Further, because $\cos^{-1}$ is monotonically decreasing, we obtain

$$i^* = \underset{i=1,\dots,n_d}{\arg\max} \ \cos\left(\beta^{(i)}\right) = \underset{i=1,\dots,n_d}{\arg\min} \ \beta^{(i)}. \tag{9}$$

This implies that we can interpret the pattern recognition algorithm as finding the smallest angle between the measured fingerprint and all fingerprints in the database, see Fig. 1. Fig. 2 illustrates the pattern recognition algorithm for a representative rubber experiment.

After identifying the most suitable i^*, the functional form of the material model is known and we compute the associated material parameters by rescaling the parameters from the database. Specifically, we identify the parameters as

$$\boldsymbol{\theta}^* = \|\hat{\boldsymbol{f}}^*\| \, \bar{\boldsymbol{\theta}}^{(i^*)} \quad \text{and} \quad \boldsymbol{\alpha}^* = \boldsymbol{\alpha}^{(i^*)}. \tag{10}$$

The pattern recognition algorithm is markedly more efficient than optimization-based model discovery methods. The computational performance of Material Fingerprinting is demonstrated in Appendix B through a comparison with the EUCLID framework (Flaschel et al., 2023).

Table 2
Summary of the discovered constitutive models for different materials. The table lists the material, the model type discovered through Material Fingerprinting, the specific model formula including fitted parameters, the average coefficient of determination R^2 across all tested experiments, and cosine similarity cs. Rubber and hydrogel are listed first, followed by the four brain regions (CX, CR, BG, CC).

Material	Discovered Model	Formula	Average R^2	cs
rubber 20 °C	Gent	$-14.0401\,[\ln(1-0.0103(I_1-3))]-p[J-1]$	0.971	0.996
rubber 50 °C	Gent	$-12.4495\,[\ln(1-0.0133(I_1-3))]-p[J-1]$	0.963	0.988
hydrogel	Mooney-Rivlin	$2.5459(I_1-3)+0.2546(I_2-3)-p[J-1]$	0.989	0.999
brain CX	Ogden	$0.0078\left[\lambda_1^{-19.1}+\lambda_2^{-19.1}+\lambda_3^{-19.1}-3\right]-p[J-1]$	0.965	0.998
brain CR	Ogden	$0.0023\left[\lambda_1^{-24.4}+\lambda_2^{-24.4}+\lambda_3^{-24.4}-3\right]-p[J-1]$	0.952	0.994
brain BG	Ogden	$0.0040\left[\lambda_1^{-18.7}+\lambda_2^{-18.7}+\lambda_3^{-18.7}-3\right]-p[J-1]$	0.980	0.997
brain CC	Ogden	$0.0012\left[\lambda_1^{-25.0}+\lambda_2^{-25.0}+\lambda_3^{-25.0}-3\right]-p[J-1]$	0.935	0.994

2.3. *Python package for Material Fingerprinting*

The previously described methods for Material Fingerprinting are implemented in Python using the `NumPy` library. Both the code and the accompanying database are distributed as an openly available, pip-installable package (Flaschel et al., 2025c). This facilitates a user-friendly application of Material Fingerprinting without having to regenerate the database. The following code demonstrates the rapid discovery of a material model for an exemplary dataset:

```
# pip install material-fingerprinting
# https://github.com/Material-Fingerprinting/material-fingerprinting
import material_fingerprinting as mf
F11_UT = np.array([1.00, 1.13, 1.41, 1.89, 2.45, 3.06, 3.62, 4.06, 4.82,
    5.41, 5.79, 6.23, 6.96, 7.25])
P11_UT = np.array([0.00, 0.136, 0.334, 0.519, 0.680, 0.866, 1.06, 1.24,
    1.60, 1.95, 2.30, 2.68, 3.78, 4.49])
m = mf.Measurement("uniaxial tension/compression", F11_UT, P11_UT)
mf.discover([m]) # or multiple measurements with mf.discover([m1,m2])
```

In the current implementation, the database is downloaded and stored locally during package installation. In future releases, we plan to host the database in the cloud to enable a more lightweight Python package. For all results presented in this work, we use Material Fingerprinting version `0.1.3` for material model discovery.

3. Experimental data

We validate our Material Fingerprinting with experimental stress-stretch/strain data for three types of soft materials: rubber, hydrogel, and brain tissue. The data for vulcanized rubber include uniaxial tension, equibiaxial tension, and pure shear tests at two temperatures, 20°C and 50°C (Treloar, 1944). The cross-linked polyacrylamide hydrogel data comprise uniaxial tension, equibiaxial tension, and pure shear tests (Yohsuke et al., 2011). Although hydrogels often exhibit rate-dependent behavior, the latter work reported negligible differences between tests at 1 mm s^{-1} and 10 mm s^{-1}, indicating quasi-static, equilibrium responses without significant viscoelastic effects. The brain tissue data include four anatomical regions – the cortex (CX), corona radiata (CR), basal ganglia (BG), and corpus callosum (CC) – with tests in uniaxial tension, uniaxial compression, and simple shear (Budday et al., 2017). While brain tissue is known to be viscoelastic, the data used here are averages of the loading and unloading curves, providing an effective quasi-static characterization suitable for model validation. All experimental stress-stretch/strain pairs are summarized in Appendix E, see Tables E.1,E.2,E.3 for rubber, hydrogel and brain data, respectively.

4. Results and discussion

As a representative example, Fig. 2 depicts the pattern recognition algorithm for the vulcanized rubber tested at 20°C. We apply this strategy to all experimental datasets.

Table 2 summarizes the discovered models, and Fig. 3 to 5 illustrate our results by directly comparing the experimental stress-stretch or stress-strain data with the discovered models from the Material Fingerprinting process. The consistent agreement across loading modes and materials highlights the ability of Material Fingerprinting to extract interpretable constitutive models directly from data without prescribing functional forms or solving nonlinear optimization problems. We assess the goodness of fit in terms of

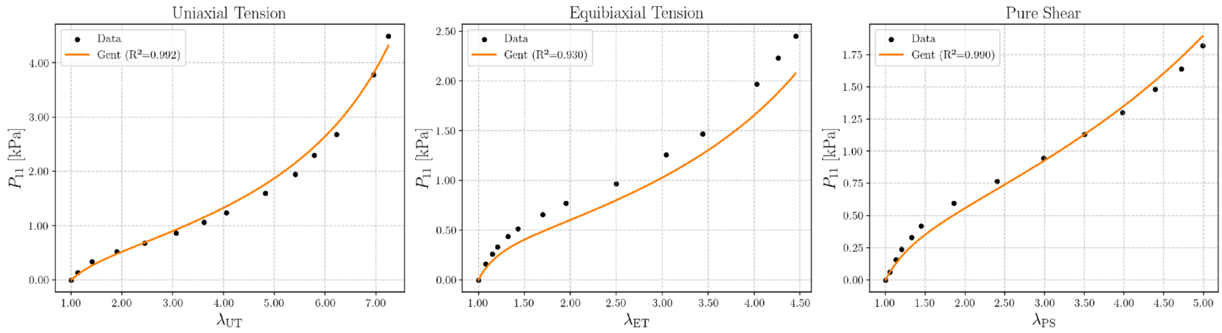

(a) Rubber at 20°C.

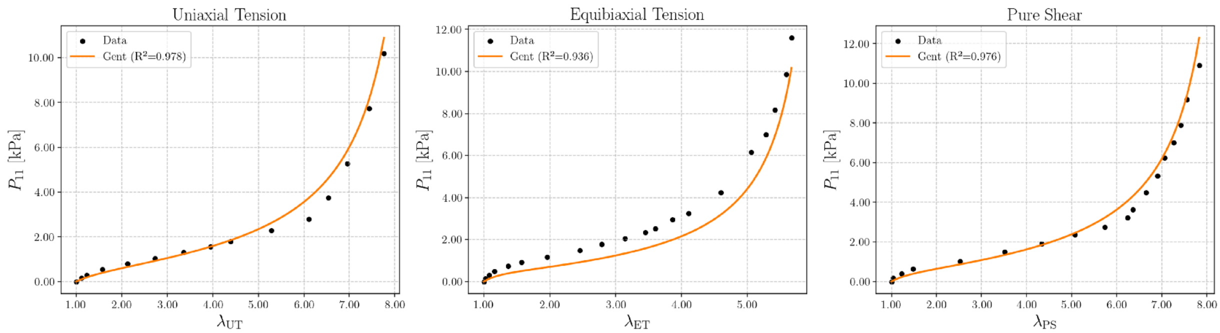

(b) Rubber at 50°C.

Fig. 3. Stress-stretch data and discovered models for rubber at two temperatures (Treloar, 1944) Experiments are performed in uniaxial tension, pure shear, and equibiaxial tension. Plots show experimental data and predictions with discovered Gent-type model. Specific model formulas are given in Table 2.

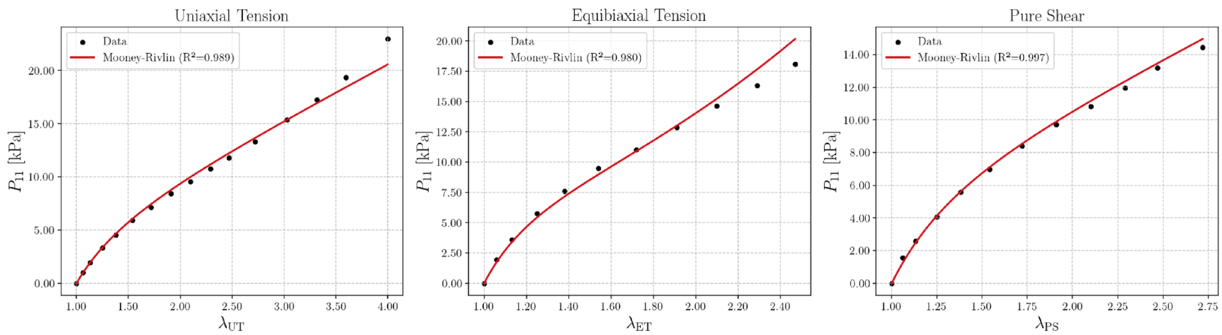

Fig. 4. Stress-stretch data and discovered models for hydrogel (Yohsuke et al., 2011). Experiments are performed in uniaxial tension, pure shear and equibiaxial tension. Plot shows experimental data and predictions with discovered Mooney-Rivlin-type model. Specific model formula is given in Table 2.

the coefficient of determination,

$$\mathrm{R}^2 = 1 - \frac{\sum_{\mathrm{k}=1}^{\mathrm{N}}\left(\mathrm{P}_{\mathrm{ij}}^{(\mathrm{k})} - \hat{\mathrm{P}}_{\mathrm{ij}}^{(\mathrm{k})}\right)^2}{\sum_{\mathrm{k}=1}^{\mathrm{N}}\left(\mathrm{P}_{\mathrm{ij}}^{(\mathrm{k})} - \overline{\mathrm{P}}_{\mathrm{ij}}\right)^2}, \tag{11}$$

where $P_{ij}^{(k)}$ denotes the experimentally measured stress component at data point k, $\overline{P}_{ij}$ is the mean value of the experimental stresses, and $\hat{P}_{ij}^{(k)}$ is the corresponding model prediction. In addition, we report the cosine similarity $\mathrm{cs} \in [-1, 1]$ according to Eq. (8).

For the vulcanized rubber tested at 20°C and 50°C, Material Fingerprinting guided the selection of a Gent-type model specified in Table 2 that closely follows the experimental measurements under uniaxial tension, pure shear, and equibiaxial loading in Fig. 3. The

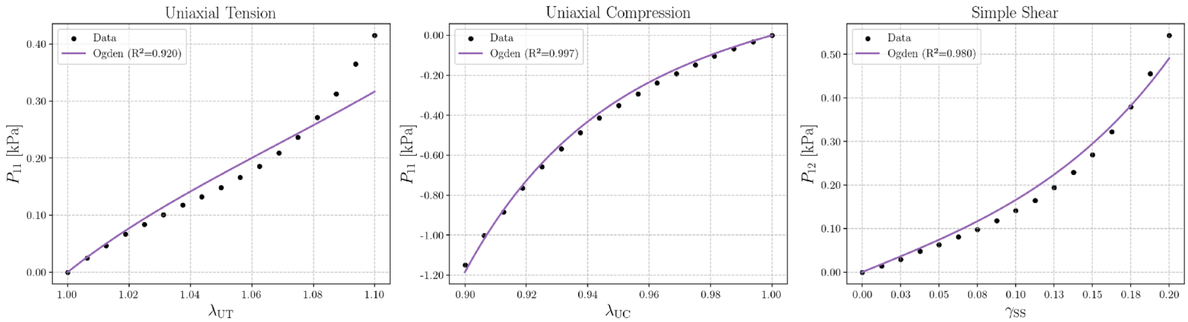

(a) Brain cortex (CX).

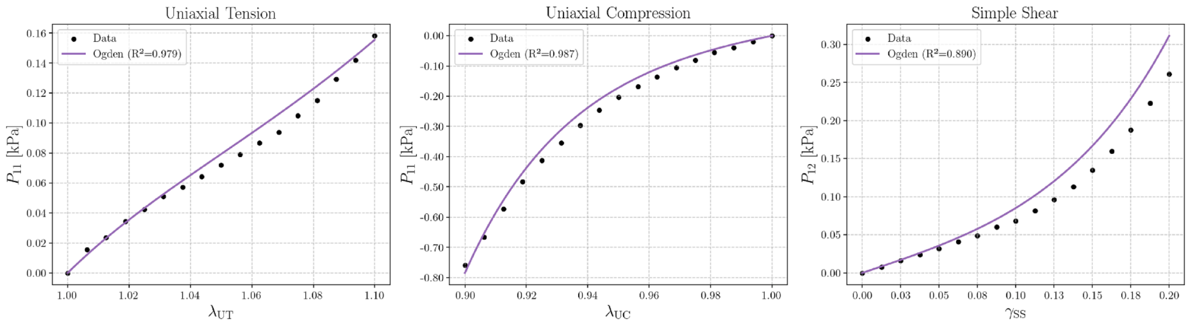

(b) Brain corona radiata (CR).

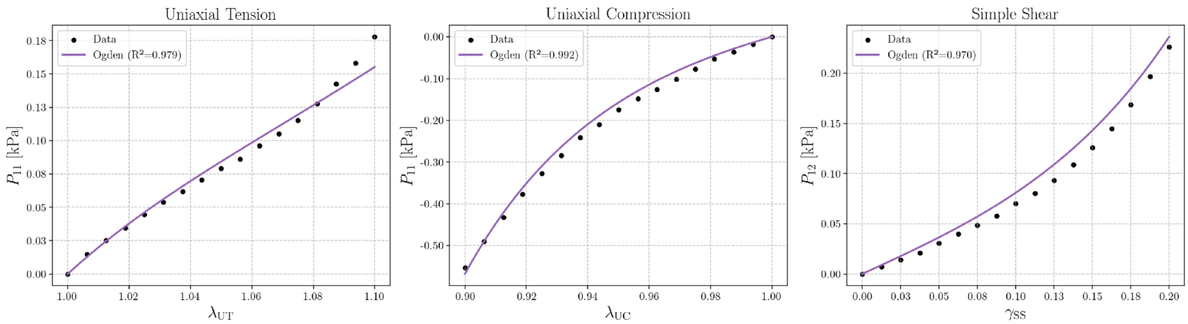

(c) Brain basal ganglia (BG).

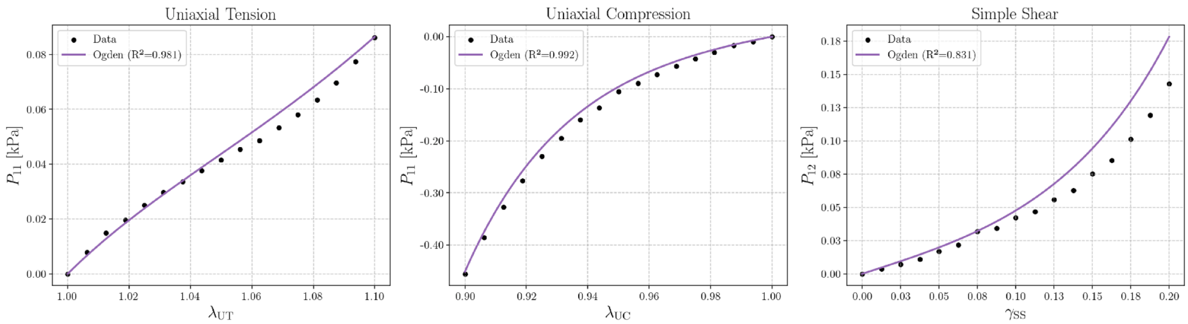

(d) Brain corpus callosum (CC).

Fig. 5. Stress-stretch and stress-strain data and discovered models for brain tissue in four regions (Budday et al., 2017). Experiments are performed in uniaxial tension, uniaxial compression, and simple shear. Plots show experimental data and predictions with discovered Ogden-type model. Specific model formulas are given in Table 2.

discovered models achieved average R^2 values of 0.973 at 20°C and 0.963 at 50°C. Neural network-based approaches (Linka and Kuhl, 2023; Sarah R. et al., 2023; Dammaß et al., 2025; Martonová et al., 2025) have reported very high accuracies for this dataset, with generalized-invariant-based constitutive neural networks reaching up to $R^2 = 0.999$ (Martonová et al., 2025). Our results are slightly below this value. However, they were obtained without solving an optimization problem or tuning network architectures. Notably, our discovered Gent model involves only two parameters, whereas the aforementioned constitutive neural networks require at least four. In addition, because of the discrete nature of our Material Fingerprinting approach, our fingerprinting material parameters will always remain discrete approximations of the parameters discovered with constitutive neural networks. We anticipate that both enriching our database with more complex models and refining the screened parameter range will yield comparable fitting performance.

For the polyacrylamide hydrogel in Fig. 4, Material Fingerprinting discovered a Mooney-Rivlin-type model specified in Table 2 with an average $R^2 = 0.991$. This relatively high value is comparable to the results produced by the recent, more complex Anssari-Benam model (Anssari-Benam, 2023), achieving a slightly higher accuracy of $R^2 = 0.999$. The key distinction is that the latter required optimization of a predefined strain energy function, while Material Fingerprinting automatically recovered a comparable formulation without preselection or parameter fitting.

For brain tissue in Fig. 5, we distinguished between cortical (CX), corona radiata (CR), basal ganglia (BG), and corpus callosum (CC) regions. For all four regions, Material Fingerprinting discovered Ogden-type incompressible hyperelastic models specified in Table 2. For the basal ganglia, the discovered model achieved the best average fit with $R^2 = 0.980$, while for the corpus callosum, the average was $R^2 = 0.935$, with somewhat reduced accuracy in the shear prediction. These findings are consistent with previous studies where constitutive models were manually selected (Miller et al., 2000; Mihai et al., 2015b, 2017; Budday et al., 2017), as well as with automatic model discovery approaches (Flaschel et al., 2023; Martonová et al., 2025), which discovered Ogden-type models with high negative exponents, but relied on solving an underlying optimization problem. In contrast, Material Fingerprinting automatically discovers the model directly from experimental data without the need for optimization, achieving comparable accuracy while simplifying the workflow and significantly reducing the time required for region-specific brain tissue characterization.

We demonstrate the differences in stress predictions among constitutive models in Appendix C by comparing the top five hyperelastic models discovered by Material Fingerprinting, using the rubber dataset at 20 °C as an example for both the full and the lower-stretch ranges. Further, we present the extrapolation behavior of Material Fingerprinting for unseen deformation modes in Appendix D. Interestingly, for all considered materials except for the brain cortex and the hydrogel, experimental data from uniaxial tension tests are sufficient to discover the most suitable model in the database via Material Fingerprinting.

Overall, the combined plots confirm that the Material Fingerprinting methodology provides a compact and discriminative representation of complex experimental data. This representation facilitates the automatic discovery of suitable constitutive models, ensuring that the predictions remain consistent with experimental responses across materials, loading modes, and environmental conditions, while offering a decisive advantage in speed and interpretability. We emphasize that both the online and offline phases require less than one second on a standard personal computer, which is orders of magnitude faster than typical optimization-based procedures.

5. Conclusions and outlook

In this work, we presented the first experimental validation of Material Fingerprinting across a diverse set of isotropic incompressible hyperelastic materials, including vulcanized rubber, hydrogels, and soft biological tissues. By interpreting stress-stretch responses as material fingerprints, the method automatically discovers suitable strain energy functions without prescribing model families or solving complex nonlinear optimization problems. The discovered models achieved excellent agreement with experimental data, with average R^2 values of 0.971 and 0.963 for rubber at two temperatures, 0.989 for hydrogel, and 0.965, 0.952, 0.980, and 0.935 for four distinct brain regions.

Our results confirm that Material Fingerprinting can recover constitutive models that are consistent with both manually calibrated formulations and advanced neural network-based discovery strategies. While neural network approaches achieve comparable accuracies, they require extensive training and parameter optimization, often resulting in black-box representations. In contrast, Material Fingerprinting discovers interpretable closed-form strain energy functions in less than a second at a fraction of the computational cost, leveraging a precomputed database that can be reused across a wide variety of experiments.

Looking forward, several avenues for extension emerge: The concept of Material Fingerprinting is not limited to the models presented in the current database and is applicable beyond isotropic hyperelasticity. It can be extended and generalized to various model combinations or to anisotropic, rate-dependent, and dissipative responses, as well as multiscale or multiphysics formulations. Increasing the breadth and resolution of fingerprint databases will further enhance model discovery, while integration with high-throughput experimental platforms could enable near real-time constitutive characterization. Finally, making the approach broadly available as an open-source Python package will democratize the method, support adoption across laboratories, and facilitate the development of a shared fingerprint repository for materials.

In summary, Material Fingerprinting provides a robust, rapid, interpretable, and broadly applicable framework for material model discovery, with the potential to complement and, in many cases, replace optimization- or neural network-based calibration strategies in computational mechanics and materials science.

Code and data availability

Accompanying this publication, we release a pip-installable Python package for supervised Material Fingerprinting, along with the generated fingerprint database (Flaschel et al., 2025c). All results presented in this work were obtained using Material Fingerprinting version `0.1.3`. Installation instructions, documentation, and examples are available on GitHub:
https://github.com/Material-Fingerprinting/material-fingerprinting.

CRediT authorship contribution statement

Denisa Martonová: Writing – original draft, Visualization, Validation, Software, Project administration, Methodology, Investigation, Formal analysis, Data curation, Conceptualization; **Ellen Kuhl:** Writing – review & editing, Supervision, Project administration, Funding acquisition, Conceptualization; **Moritz Flaschel:** Writing – original draft, Visualization, Validation, Software, Project administration, Methodology, Investigation, Formal analysis, Conceptualization.

Declaration of competing interest

The authors, Denisa Martonová, Ellen Kuhl, and Moritz Flaschel declare no conflict of interest regarding the manuscript entitled "Material Fingerprinting for rapid discovery of hyperelastic models: First experimental validation".

Acknowledgments

The authors acknowledge support from the National Science Foundation (NSF) CMMI Award 2,320,933 and from the European Research Council (ERC) Grant 101,141,626 DISCOVER funded by the European Union. Views and opinions expressed are, however, those of the authors only and do not necessarily reflect those of the European Union or the European Research Council Executive Agency. Neither the European Union nor the granting authority can be held responsible for them.

Appendix A. Stress components for incompressible load cases

In the following, we summarize the stress responses computed for all material models under the different load cases (Flaschel et al., 2025b). We consider an incompressible, isotropic hyperelastic solid with isochoric strain energy

$$W = \tilde{W}(I_1, I_2) - p[J-1] \quad \text{or} \quad W = \tilde{W}(\lambda_1, \lambda_2, \lambda_3) - p[J-1],$$

where $I_1 = \mathrm{tr}(\boldsymbol{C})$ and $I_2 = \frac{1}{2}[\mathrm{tr}(\boldsymbol{C})^2 - \mathrm{tr}\left(\boldsymbol{C}^2\right)]$ are the first and second invariants of the right Cauchy-Green deformation tensor $\boldsymbol{C} = \boldsymbol{F}^T \boldsymbol{F}$, and λ_i are the principal stretches, that is, the square roots of the eigenvalues of $\boldsymbol{C}$. For all load cases, we compute the Lagrange multiplier p by leveraging the constraint $P_{33} = 0$.

For the invariant-based models, the first Piola stress reads

$$\boldsymbol{P} = \frac{\partial \tilde{W}}{\partial \boldsymbol{F}} - p\,\boldsymbol{F}^{-T} = \frac{\partial \tilde{W}}{\partial I_1}\frac{\partial I_1}{\partial \boldsymbol{F}} + \frac{\partial \tilde{W}}{\partial I_2}\frac{\partial I_2}{\partial \boldsymbol{F}} - p\,\boldsymbol{F}^{-T}.$$

The invariant derivatives are

$$\frac{\partial I_1}{\partial \boldsymbol{F}} = 2\boldsymbol{F}, \qquad \frac{\partial I_2}{\partial \boldsymbol{F}} = 2\left(I_1 \boldsymbol{F} - \boldsymbol{F}\boldsymbol{C}\right).$$

We obtain the following formulas for the first and second invariants under the different loading conditions:

Uniaxial tension/compression (UT).

$$\boldsymbol{F}_{\mathrm{UT}} = \mathrm{diag}(\lambda_{\mathrm{UT}}, \lambda_{\mathrm{UT}}^{-1/2}, \lambda_{\mathrm{UT}}^{-1/2}), \quad \boldsymbol{C}_{\mathrm{UT}} = \mathrm{diag}(\lambda_{\mathrm{UT}}^{2}, \lambda_{\mathrm{UT}}^{-1}, \lambda_{\mathrm{UT}}^{-1}),$$

$$I_1^{\mathrm{UT}} = \lambda_{\mathrm{UT}}^2 + 2\lambda_{\mathrm{UT}}^{-1}, \quad I_2^{\mathrm{UT}} = \lambda_{\mathrm{UT}}^{-2} + 2\lambda_{\mathrm{UT}}.$$

Equi-biaxial tension/compression (ET).

$$\boldsymbol{F}_{\mathrm{ET}} = \mathrm{diag}(\lambda_{\mathrm{ET}}, \lambda_{\mathrm{ET}}, \lambda_{\mathrm{ET}}^{-2}), \quad \boldsymbol{C}_{\mathrm{ET}} = \mathrm{diag}(\lambda_{\mathrm{ET}}^{2}, \lambda_{\mathrm{ET}}^{2}, \lambda_{\mathrm{ET}}^{-4}),$$

$$I_1^{\mathrm{ET}} = 2\lambda_{\mathrm{ET}}^2 + \lambda_{\mathrm{ET}}^{-4}, \quad I_2^{\mathrm{ET}} = 2\lambda_{\mathrm{ET}}^{-2} + \lambda_{\mathrm{ET}}^{4}.$$

Pure shear (PS).

$$\boldsymbol{F}_{\mathrm{PS}} = \mathrm{diag}(\lambda_{\mathrm{PS}}, 1, \lambda_{\mathrm{PS}}^{-1}), \quad \boldsymbol{C}_{\mathrm{PS}} = \mathrm{diag}(\lambda_{\mathrm{PS}}^{2}, 1, \lambda_{\mathrm{PS}}^{-2}),$$

$$I_1^{\mathrm{PS}} = I_2^{\mathrm{PS}} = 1 + \lambda_{\mathrm{PS}}^2 + \lambda_{\mathrm{PS}}^{-2}.$$

Simple shear (SS).

$$\boldsymbol{F}_{\mathrm{SS}} = \begin{bmatrix} 1 & \gamma_{\mathrm{SS}} & 0 \\ 0 & 1 & 0 \\ 0 & 0 & 1 \end{bmatrix}, \quad \boldsymbol{C}_{\mathrm{SS}} = \begin{bmatrix} 1 & \gamma_{\mathrm{SS}} & 0 \\ \gamma_{\mathrm{SS}} & 1+\gamma_{\mathrm{SS}}^2 & 0 \\ 0 & 0 & 1 \end{bmatrix}, \quad I_1^{\mathrm{SS}} = I_2^{\mathrm{SS}} = 3 + \gamma_{\mathrm{SS}}^2.$$

Writing $P_{11} = P_{\mathrm{ET}}$ in uniaxial tension/compression, $P_{11} = P_{22} = P_{\mathrm{ET}}$ in equibiaxial tension, $P_{11} = P_{\mathrm{PS}}$ in pure shear, and $P_{12} = P_{\mathrm{SS}}$ in simple shear, the invariant derivatives and stress components for the following considered models are:

Blatz–Ko.

$$W = \theta_1[I_2 - 3] - p[J-1], \quad \frac{\partial \tilde{W}}{\partial I_2} = \theta_1, \quad \frac{\partial \tilde{W}}{\partial I_1} = 0,$$

$$P_{\mathrm{UT}} = 2\theta_1(1 - \lambda_{\mathrm{UT}}^{-3}), \qquad P_{\mathrm{ET}} = 2\theta_1(\lambda_{\mathrm{ET}}^3 - \lambda_{\mathrm{ET}}^{-3}),$$
$$P_{\mathrm{PS}} = 2\theta_1(\lambda_{\mathrm{PS}} - \lambda_{\mathrm{PS}}^{-3}), \quad P_{\mathrm{SS}} = 2\theta_1\gamma_{\mathrm{SS}}.$$

Demiray.

$$W = \theta_2[\exp\big(\alpha_2(I_1 - 3)\big) - 1] - p[J-1], \quad \frac{\partial \tilde{W}}{\partial I_1} = \theta_2\alpha_2 e^{\alpha_2(I_1-3)}, \quad \frac{\partial \tilde{W}}{\partial I_2} = 0,$$

$$P_{\mathrm{UT}} = 2(\lambda_{\mathrm{UT}} - \lambda_{\mathrm{UT}}^{-2})\theta_2\alpha_2 e^{\alpha_2(I_1^{\mathrm{UT}}-3)}, \quad P_{\mathrm{ET}} = 2(\lambda_{\mathrm{ET}} - \lambda_{\mathrm{ET}}^{-5})\theta_2\alpha_2 e^{\alpha_2(I_1^{\mathrm{ET}}-3)},$$
$$P_{\mathrm{PS}} = 2(\lambda_{\mathrm{PS}} - \lambda_{\mathrm{PS}}^{-3})\theta_2\alpha_2 e^{\alpha_2(I_1^{\mathrm{PS}}-3)}, \quad P_{\mathrm{SS}} = 2\gamma_{\mathrm{SS}}\theta_2\alpha_2 e^{\alpha_2(I_1^{\mathrm{SS}}-3)}.$$

Gent.

$$W = -\theta_3 \ln\big(1 - \alpha_3[I_1 - 3]\big) - p[J-1], \quad \frac{\partial \tilde{W}}{\partial I_1} = \frac{\theta_3\alpha_3}{1 - \alpha_3(I_1-3)}, \quad \frac{\partial \tilde{W}}{\partial I_2} = 0,$$

$$P_{\mathrm{UT}} = 2(\lambda_{\mathrm{UT}} - \lambda_{\mathrm{UT}}^{-2})\frac{\theta_3\alpha_3}{1-\alpha_3(I_1^{\mathrm{UT}}-3)}, \quad P_{\mathrm{ET}} = 2(\lambda_{\mathrm{ET}} - \lambda_{\mathrm{ET}}^{-5})\frac{\theta_3\alpha_3}{1-\alpha_3(I_1^{\mathrm{ET}}-3)},$$
$$P_{\mathrm{PS}} = 2(\lambda_{\mathrm{PS}} - \lambda_{\mathrm{PS}}^{-3})\frac{\theta_3\alpha_3}{1-\alpha_3(I_1^{\mathrm{PS}}-3)}, \quad P_{\mathrm{SS}} = 2\gamma_{\mathrm{SS}}\frac{\theta_3\alpha_3}{1-\alpha_3(I_1^{\mathrm{SS}}-3)}.$$

Holzapfel-type.

$$W = \theta_4[\exp\big(\alpha_4[I_1 - 3]^2\big) - 1] - p[J-1], \quad \frac{\partial \tilde{W}}{\partial I_1} = 2\theta_4\alpha_4(I_1-3)e^{\alpha_4(I_1-3)^2}, \quad \frac{\partial \tilde{W}}{\partial I_2} = 0,$$

$$P_{\mathrm{UT}} = 4\theta_4\alpha_4(I_1^{\mathrm{UT}} - 3)(\lambda_{\mathrm{UT}} - \lambda_{\mathrm{UT}}^{-2})e^{\alpha_4(I_1^{\mathrm{UT}}-3)^2},$$
$$P_{\mathrm{ET}} = 4\theta_4\alpha_4(I_1^{\mathrm{ET}} - 3)(\lambda_{\mathrm{ET}} - \lambda_{\mathrm{ET}}^{-5})e^{\alpha_4(I_1^{\mathrm{ET}}-3)^2},$$
$$P_{\mathrm{PS}} = 4\theta_4\alpha_4(I_1^{\mathrm{PS}} - 3)(\lambda_{\mathrm{PS}} - \lambda_{\mathrm{PS}}^{-3})e^{\alpha_4(I_1^{\mathrm{PS}}-3)^2},$$
$$P_{\mathrm{SS}} = 4\theta_4\alpha_4(I_1^{\mathrm{SS}} - 3)\gamma_{\mathrm{SS}}e^{\alpha_4(I_1^{\mathrm{SS}}-3)^2}.$$

Mooney-Rivlin.

$$W = \theta_5[I_1 - 3] + \theta_1[I_2 - 3] - p[J-1], \quad \frac{\partial \tilde{W}}{\partial I_1} = \theta_5, \quad \frac{\partial \tilde{W}}{\partial I_2} = \theta_1,$$

$$P_{\mathrm{UT}} = 2\theta_5(\lambda_{\mathrm{UT}} - \lambda_{\mathrm{UT}}^{-2}) + 2\theta_1(1 - \lambda_{\mathrm{UT}}^{-3}), \quad P_{\mathrm{ET}} = 2\theta_5(\lambda_{\mathrm{ET}} - \lambda_{\mathrm{ET}}^{-5}) + 2\theta_1(\lambda_{\mathrm{ET}}^3 - \lambda_{\mathrm{ET}}^{-3}),$$
$$P_{\mathrm{PS}} = 2(\theta_5 + \theta_1)(\lambda_{\mathrm{PS}} - \lambda_{\mathrm{PS}}^{-3}), \qquad P_{\mathrm{SS}} = 2(\theta_5 + \theta_1)\gamma_{\mathrm{SS}}.$$

Neo-Hooke.

$$W = \theta_5[I_1 - 3] - p[J-1], \quad \frac{\partial \tilde{W}}{\partial I_1} = \theta_5, \quad \frac{\partial \tilde{W}}{\partial I_2} = 0,$$

$$P_{\mathrm{UT}} = 2\theta_5(\lambda_{\mathrm{UT}} - \lambda_{\mathrm{UT}}^{-2}), \quad P_{\mathrm{ET}} = 2\theta_5(\lambda_{\mathrm{ET}} - \lambda_{\mathrm{ET}}^{-5}),$$
$$P_{\mathrm{PS}} = 2\theta_5(\lambda_{\mathrm{PS}} - \lambda_{\mathrm{PS}}^{-3}), \quad P_{\mathrm{SS}} = 2\theta_5\gamma_{\mathrm{SS}}.$$

For the stretch-based models, the first Piola stress reads

$$\boldsymbol{P} = \frac{\partial \tilde{W}}{\partial \boldsymbol{F}} - p\,\boldsymbol{F}^{-T} = \sum_i \frac{\partial \tilde{W}}{\partial \lambda_i}\frac{\partial \lambda_i}{\partial \boldsymbol{F}} - p\,\boldsymbol{F}^{-T}.$$

Ogden (one-term).

$$W = \theta_6[\lambda_1^{\alpha_6} + \lambda_2^{\alpha_6} + \lambda_3^{\alpha_6} - 3] - p[J-1], \quad \frac{\partial \tilde{W}}{\partial \lambda_i} = \theta_6 \alpha_6 \lambda_i^{\alpha_6 - 1},$$

$$\begin{aligned}
P_{\mathrm{UT}} &= \theta_6\alpha_6(\lambda_{\mathrm{UT}}^{\alpha_6-1} - \lambda_{\mathrm{UT}}^{-(\alpha_6/2+1)}),\\
P_{\mathrm{ET}} &= \theta_6\alpha_6(\lambda_{\mathrm{ET}}^{\alpha_6-1} - \lambda_{\mathrm{ET}}^{-(2\alpha_6+1)}),\\
P_{\mathrm{PS}} &= \theta_6\alpha_6(\lambda_{\mathrm{PS}}^{\alpha_6-1} - \lambda_{\mathrm{PS}}^{-(\alpha_6+1)}),\\
P_{\mathrm{SS}} &= \theta_6\alpha_6\left(\lambda_1^{\alpha_6-1}\frac{\partial\lambda_1}{\partial\gamma_{\mathrm{SS}}} + \lambda_2^{\alpha_6-1}\frac{\partial\lambda_2}{\partial\gamma_{\mathrm{SS}}}\right),
\end{aligned}$$

$$\lambda_{1,2} = \sqrt{\frac{2+\gamma_{\mathrm{SS}}^2 \pm \gamma_{\mathrm{SS}}\sqrt{\gamma_{\mathrm{SS}}^2+4}}{2}} \quad \text{and} \quad \frac{\partial\lambda_{1,2}}{\partial\gamma_{\mathrm{SS}}} = \frac{\gamma_{\mathrm{SS}}\sqrt{4+\gamma_{\mathrm{SS}}^2} \pm (4+\gamma_{\mathrm{SS}}^2)}{2(4+\gamma_{\mathrm{SS}}^2)}.$$

Appendix B. Computational efficiency

To assess the computational efficiency of the supervised Material Fingerprinting framework, we consider a representative numerically generated dataset and compare its computational time to that of EUCLID, an optimization-based approach for material model discovery (Flaschel et al., 2021, 2023; Abbasi et al., 2025). EUCLID discovers suitable constitutive models by defining a library of candidate material features and solving an L_p-regularized regression problem (Frank and Friedman, 1993; Tibshirani, 1996; Efron et al., 2004) to select the most relevant terms for describing the observed data.

A direct comparison between Material Fingerprinting and EUCLID is challenging, since EUCLID's computational cost depends strongly on the size and structure of the material model library, the choice of the hyperparameter p, and the employed numerical solver. When the model library depends linearly on the parameters and $p = 1$, the L_1-regularized EUCLID problem can be solved efficiently using a coordinate descent algorithm (Flaschel et al., 2025a). In contrast, for nonlinear libraries, the EUCLID problem typically requires discretization of the parameter space (Flaschel et al., 2023) or iterative optimization methods such as the Iterative Soft-Thresholding Algorithm (ISTA) (Flaschel et al., 2025a).

To provide a representative benchmark, we reproduce a synthetic example (Flaschel et al., 2025a). Specifically, we generate synthetic data for the Ogden model with $\theta_6 = 2.0$ and $\alpha_6 = 3.0$, consisting of 50 data points for uniaxial tension over stretches between 1.0 and 1.5, and 50 data points for simple shear over shear strains between 0 and 0.5. No noise is added to the data. Using this dataset, Material Fingerprinting successfully rediscovers the correct material model in less than 0.1 s on a standard laptop.

For comparison, we apply supervised EUCLID using ISTA to solve the corresponding optimization problem. The material model library includes both Mooney-Rivlin and Ogden terms. We set $p = 1$, use a sparsity-promoting regularization parameter of 1.0, and select a step size of 0.0001. Under these settings, EUCLID correctly discovers the Ogden model in approximately 10 s on the same hardware. Thus, for this example, Material Fingerprinting achieves a roughly two orders of magnitude speed-up compared to EUCLID. We note, however, that, as mentioned previously, depending on the model library and the chosen solver, EUCLID may require significantly different computational times, particularly if the fast coordinate descent algorithm can be applied.

Finally, we note that the advantages of Material Fingerprinting are expected to be even more pronounced in the unsupervised setting (Flaschel et al., 2025b), where it has been shown to outperform conventional approaches such as Finite Element Model Updating by several orders of magnitude.

Table B.1
Top five discovered constitutive models for rubber at 20 °C, comparing full- and lower-stretch ranges. The values represent the maximum cosine similarity $\mathrm{cs}_{\max}$ between the experimental fingerprint and all fingerprints generated for each model. The cosine similarity quantifies the agreement between model predictions and experimental data, with $\mathrm{cs}_{\max}$ indicating the best match achieved by each model.

Top models	Rubber 20°C (full-stretch range)		Rubber 20°C (lower-stretch range)	
	Model	$\mathrm{cs}_{\max}$	**Model**	$\mathrm{cs}_{\max}$
1	Gent	0.996	Mooney-Rivlin	0.999
2	Ogden	0.987	Ogden	0.999
3	Neo-Hooke	0.978	Neo-Hooke	0.996
4	Mooney-Rivlin	0.934	Gent	0.995
5	Demiray	0.751	Demiray	0.936

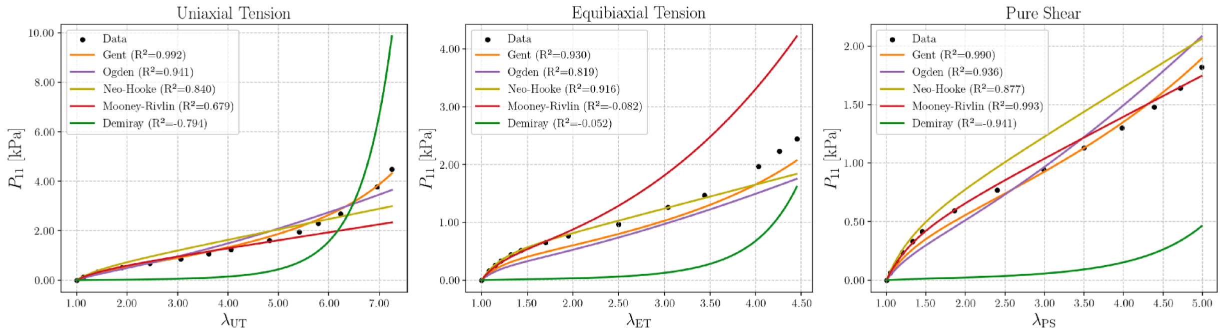

(a)

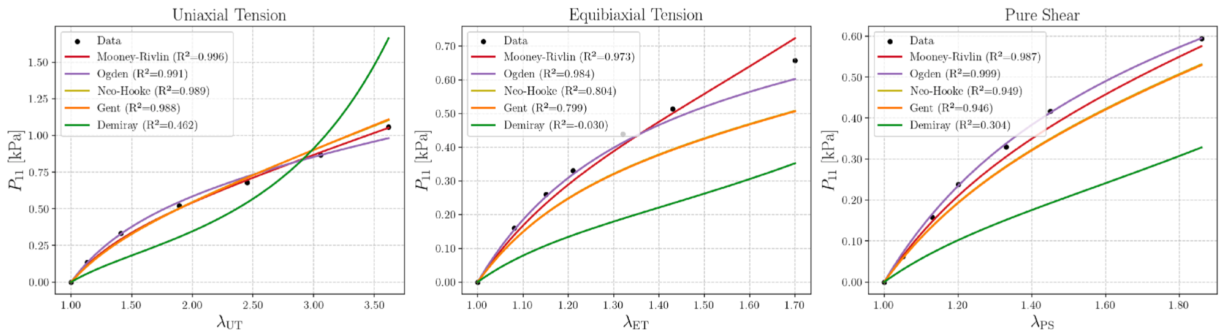

(b)

Fig. B.1. **C**omparison of top five discovered models for rubber at **20**°C for (a) full-stretch range and (b) lower-stretch ranges. Each subplot shows the experimental data (black dots) and the predictions from the five top-ranked hyperelastic models in the database (Table 1) discovered through Material Fingerprinting. The coefficient of determination R^2 quantifies the model-data agreement for each experimental mode.

Appendix C. Model similarity

Depending on the available experimental data, multiple models in the database may be capable of reproducing the measurements. In the following, we investigate the cosine similarity and fitting accuracy of different models in the database exemplarily for the rubber dataset at 20 °C. We consider two scenarios; one in which we use the full dataset, and another in which we include only approximately half of the stretch ranges. Table B.1 reports the maximum cosine similarities $\mathrm{cs}_{\max}$ obtained for the top five material models in the database. For the full dataset, the Material Fingerprinting method clearly identifies the Gent model as the best-performing model, yielding the highest cosine similarity. However, when we consider only the lower-stretch range, several models achieve identical cosine similarities. This is expected, as many hyperelastic models become indistinguishable at small stretches. Finally, Fig. B.1 presents the stress-stretch/strain data together with the predictions of the top five hyperelastic models. As anticipated, when we use only half of the stretch range, more models are able to fit the data. A similar trend is expected for optimization-based model discovery methods, which likewise require sufficient data coverage, especially in the nonlinear regime, to achieve reliable and unique model discovery.

Appendix D. Extrapolation behavior

To examine the extrapolation behavior of the discovered models for the considered datasets, we investigate whether experimental data from uniaxial tension tests alone are sufficient to discover the same constitutive model as when all available loading modes are used, see Figs. 3–5. For each material dataset (rubber at two temperatures, hydrogel, and four brain regions), we apply Material Fingerprinting using only the uniaxial tension data as input for model discovery. We then evaluate the predictions of the discovered model against the unseen data. Whenever the discovered model deviates from the one obtained using the full dataset, we add an additional testing mode as input for Material Fingerprinting.

Figs. D.1–D.3 illustrate, for each material, the loading modes that are required to discover the same model as obtained with the full dataset. For all considered materials except for the brain cortex and the hydrogel, uniaxial tension data are sufficient to discover the most suitable model via Material Fingerprinting. For the brain cortex, uniaxial tension and compression data are required to discover the most suitable model. For the hydrogel, uniaxial tension and equibiaxial tension data are required to discover the most suitable model.

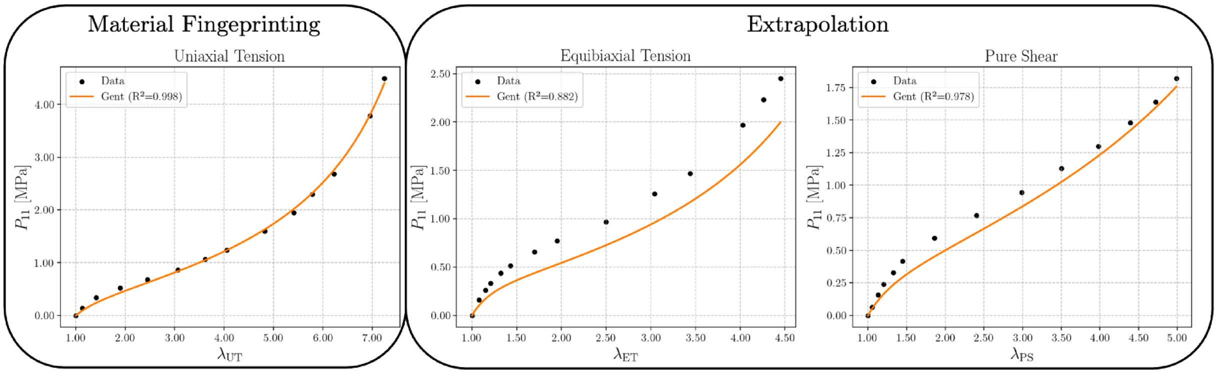

(a) Rubber at 20°C.

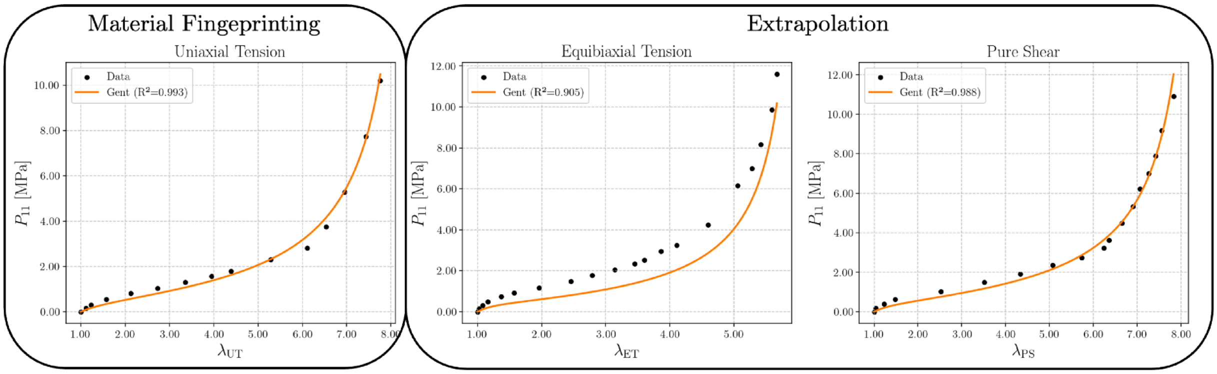

(b) Rubber at 50°C.

Fig. D.1. Stress-stretch data and discovered models for rubber at two temperatures (Treloar, 1944). Uniaxial tension tests are used for model discovery with Material Fingerprinting whereas equibiaxial tension and pure shear data are unseen. Plots show experimental data and predictions with discovered Gent-type model.

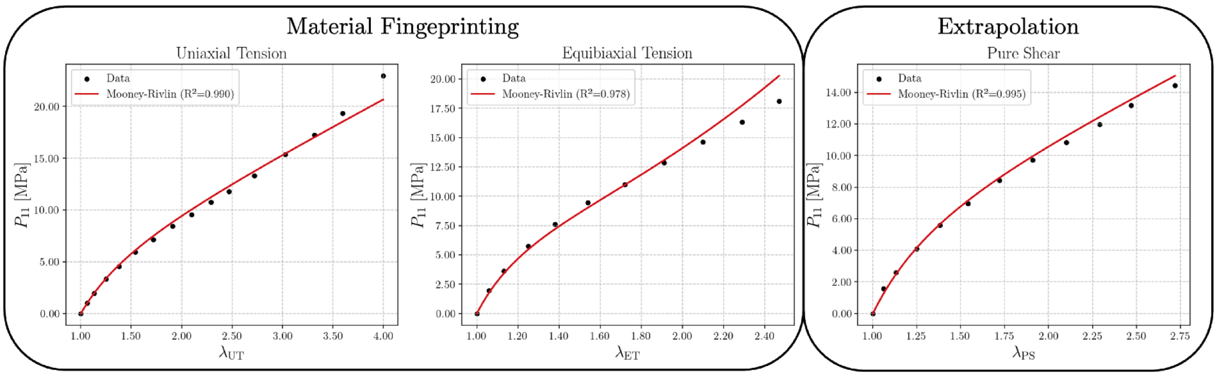

Fig. D.2. Stress-stretch data and discovered models for hydrogel (Yohsuke et al., 2011). Uniaxial and equibiaxial tension tests are used for model discovery with Material Fingerprinting whereas pure shear data are unseen. Plot shows experimental data and predictions with discovered Mooney-Rivlin-type model.

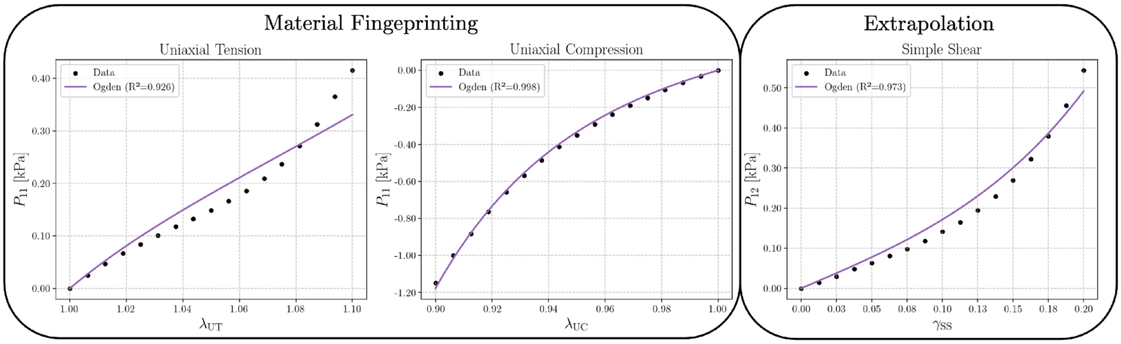

(a) Brain cortex (CX).

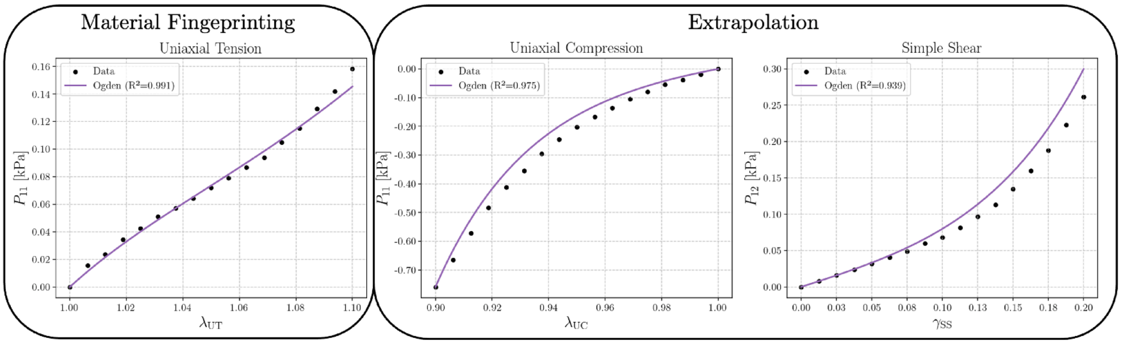

(b) Brain corona radiata (CR).

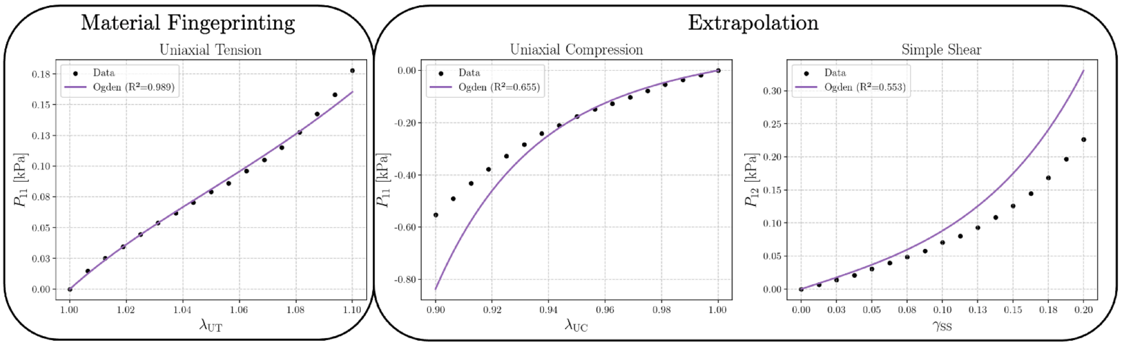

(c) Brain basal ganglia (BG).

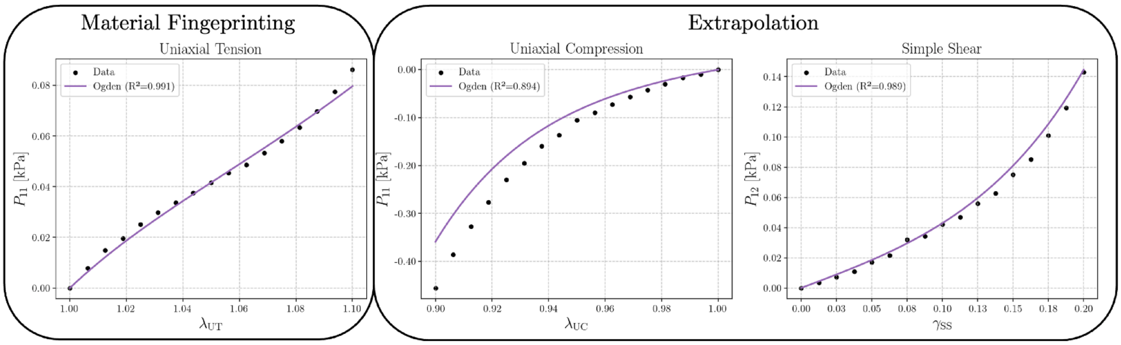

(d) Brain corpus callosum (CC).

Fig. D.3. Stress-stretch and stress-strain data and discovered models for brain tissue in four regions (Budday et al., 2017). For brain CX, uniaxial and compression tension tests are used for model discovery with Material Fingerprinting and simple shear data are unseen. For brain CR, BG, and CC, solely uniaxial tension tests are used for model discovery with Material Fingerprinting whereas uniaxial compression and simple shear data are unseen. Plots show experimental data and predictions with discovered Ogden-type model.

Appendix E. Experimental data

Table E.1
Nominal stress vs. stretch data for rubber (Treloar, 1944). First Piola stress P_{11} in MPa.

Rubber 20 °C						Rubber 50 °C					
UT		ET		PS		UT		ET		PS	
λ_{UT}	P_{11}	λ_{ET}	P_{11}	λ_{PS}	P_{11}	λ_{UT}	P_{11}	λ_{ET}	P_{11}	λ_{PS}	P_{11}
1.00	0.000	1.00	0.000	1.00	0.000	1.00	0.000	1.00	0.000	1.00	0.000
1.13	0.136	1.08	0.160	1.05	0.063	1.11	0.165	1.02	0.147	1.04	0.170
1.41	0.334	1.15	0.260	1.13	0.158	1.23	0.289	1.08	0.298	1.23	0.399
1.89	0.519	1.21	0.331	1.20	0.238	1.57	0.537	1.16	0.478	1.48	0.627
2.45	0.680	1.32	0.439	1.33	0.330	2.12	0.805	1.37	0.743	2.52	1.030
3.06	0.866	1.43	0.514	1.45	0.417	2.73	1.030	1.57	0.921	3.51	1.490
3.62	1.060	1.70	0.657	1.86	0.594	3.36	1.300	1.96	1.170	4.33	1.900
4.06	1.240	1.95	0.773	2.40	0.767	3.95	1.570	2.46	1.490	5.07	2.360
4.82	1.600	2.50	0.968	2.99	0.945	4.39	1.790	2.79	1.780	5.74	2.740
5.41	1.950	3.04	1.260	3.50	1.130	5.29	2.290	3.14	2.040	6.24	3.220
5.79	2.300	3.44	1.470	3.98	1.300	6.11	2.800	3.45	2.330	6.36	3.630
6.23	2.680	4.03	1.970	4.39	1.480	6.54	3.750	3.60	2.530	6.65	4.490
6.96	3.780	4.26	2.230	4.72	1.640	6.95	5.270	3.86	2.960	6.91	5.340
7.25	4.490	4.45	2.450	4.99	1.820	7.43	7.730	4.11	3.240	7.06	6.230
–	–	–	–	–	–	7.76	10.200	4.60	4.240	7.26	7.000
–	–	–	–	–	–	–	–	5.06	6.150	7.42	7.890
–	–	–	–	–	–	–	–	5.28	6.990	7.56	9.180
–	–	–	–	–	–	–	–	5.42	8.180	7.83	10.900
–	–	–	–	–	–	–	–	5.59	9.870	–	–
–	–	–	–	–	–	–	–	5.67	11.600	–	–

Table E.2
Nominal stress vs. stretch data for PAAm hydrogel (Yohsuke et al., 2011). First Piola stress P_{11} in MPa.

Hydrogel					
UT		ET		PS	
λ_{UT}	P_{11}	λ_{ET}	P_{11}	λ_{PS}	P_{11}
1.00	0.000	1.00	0.000	1.00	0.000
1.06	1.019	1.06	1.943	1.06	1.575
1.13	1.947	1.13	3.615	1.13	2.593
1.25	3.340	1.25	5.752	1.25	4.080
1.38	4.551	1.38	7.616	1.38	5.572
1.54	5.948	1.54	9.481	1.54	6.968
1.72	7.116	1.72	11.000	1.72	8.413
1.91	8.421	1.91	12.864	1.91	9.717
2.10	9.543	2.10	14.638	2.10	10.838
2.29	10.755	2.29	16.319	2.29	11.961
2.47	11.781	2.47	18.089	2.47	13.174
2.72	13.320	–	–	2.72	14.430
3.03	15.373	–	–	–	–
3.32	17.238	–	–	–	–
3.60	19.331	–	–	–	–
4.00	22.963	–	–	–	–

Table E.3
Nominal stress vs. stretch and shear strain data for brain tissue (Budday et al., 2017). Cortex, corona radiata, basal ganglia, and corpus callosum. First Piola stress components P_{11} and P_{12} in kPa.

Cortex						Corona radiata					
UC		UT		SS		UC		UT		SS	
λ_{UT}	P_{11}	λ_{UC}	P_{11}	γ_{SS}	P_{12}	λ_{UT}	P_{11}	λ_{UC}	P_{11}	γ_{SS}	P_{12}
1.00	0.000	0.90	−1.148	0.00	0.000	1.00	0.000	0.90	−0.759	0.00	0.000
1.01	0.025	0.91	−1.001	0.01	0.015	1.01	0.016	0.91	−0.666	0.01	0.008
1.01	0.046	0.91	−0.884	0.03	0.029	1.01	0.024	0.91	−0.572	0.03	0.016
1.02	0.067	0.92	−0.763	0.04	0.049	1.02	0.035	0.92	−0.483	0.04	0.024
1.03	0.084	0.93	−0.658	0.05	0.063	1.03	0.051	0.93	−0.413	0.05	0.032
1.03	0.101	0.93	−0.568	0.06	0.081	1.03	0.057	0.93	−0.354	0.06	0.041
1.04	0.118	0.94	−0.487	0.08	0.098	1.04	0.064	0.94	−0.296	0.08	0.049
1.04	0.132	0.94	−0.413	0.09	0.119	1.04	0.072	0.94	−0.245	0.09	0.060
1.05	0.149	0.95	−0.350	0.10	0.141	1.05	0.079	0.95	−0.202	0.10	0.068
1.06	0.166	0.96	−0.292	0.11	0.165	1.06	0.087	0.96	−0.167	0.11	0.082
1.06	0.186	0.96	−0.238	0.13	0.194	1.06	0.094	0.96	−0.136	0.13	0.096
1.07	0.209	0.97	−0.191	0.14	0.229	1.07	0.105	0.97	−0.105	0.14	0.113
1.08	0.237	0.98	−0.148	0.15	0.270	1.08	0.115	0.98	−0.080	0.15	0.135
1.08	0.271	0.98	−0.104	0.16	0.323	1.08	0.129	0.98	−0.054	0.16	0.160
1.09	0.313	0.99	−0.066	0.18	0.379	1.09	0.142	0.99	−0.039	0.18	0.188
1.09	0.365	0.99	−0.031	0.19	0.456	1.09	0.158	0.99	−0.019	0.19	0.223
1.10	0.415	1.00	0.000	0.20	0.544	1.10	0.178	1.00	0.000	0.20	0.261

Basal ganglia						Corpus callosum					
UC		UT		SS		UC		UT		SS	
λ_{UT}	P_{11}	λ_{UC}	P_{11}	γ_{SS}	P_{12}	λ_{UT}	P_{11}	λ_{UC}	P_{11}	γ_{SS}	P_{12}
1.00	0.000	0.90	−0.553	0.00	0.000	1.00	0.000	0.90	−0.456	0.00	0.000
1.01	0.015	0.91	−0.491	0.01	0.007	1.01	0.008	0.91	−0.385	0.01	0.004
1.01	0.025	0.91	−0.432	0.03	0.014	1.01	0.015	0.91	−0.327	0.03	0.007
1.02	0.035	0.92	−0.378	0.04	0.021	1.02	0.020	0.92	−0.276	0.04	0.011
1.03	0.045	0.93	−0.327	0.05	0.031	1.03	0.025	0.93	−0.230	0.05	0.017
1.03	0.054	0.93	−0.284	0.06	0.040	1.03	0.030	0.93	−0.195	0.06	0.022
1.04	0.062	0.94	−0.241	0.08	0.049	1.04	0.034	0.94	−0.160	0.08	0.032
1.04	0.071	0.94	−0.210	0.09	0.058	1.04	0.038	0.94	−0.136	0.09	0.034
1.05	0.079	0.95	−0.175	0.10	0.070	1.05	0.042	0.95	−0.105	0.10	0.042
1.06	0.086	0.96	−0.148	0.11	0.081	1.06	0.045	0.96	−0.089	0.11	0.047
1.06	0.096	0.96	−0.127	0.13	0.093	1.06	0.049	0.96	−0.073	0.13	0.056
1.07	0.105	0.97	−0.102	0.14	0.109	1.07	0.053	0.97	−0.056	0.14	0.063
1.08	0.115	0.98	−0.078	0.15	0.126	1.08	0.058	0.98	−0.043	0.15	0.075
1.08	0.128	0.98	−0.053	0.16	0.145	1.08	0.063	0.98	−0.030	0.16	0.085
1.09	0.143	0.99	−0.036	0.18	0.169	1.09	0.070	0.99	−0.016	0.18	0.101
1.09	0.158	0.99	−0.017	0.19	0.197	1.09	0.078	0.99	−0.010	0.19	0.119
1.10	0.178	1.00	0.000	0.20	0.226	1.10	0.086	1.00	0.000	0.20	0.143

References

Abbasi, A., Ricci, M., Carrara, P., Flaschel, M., Kumar, S., Marfia, S., Lorenzis, L.D., et al., 2025. Discovery of hyperelastic constitutive laws from experimental data with euclid. https://doi.org/10.48550/arXiv.2510.24747

Abdolazizi, K.P., Aydin, R.C., Cyron, C.J., Linka, K., et al., 2025. Constitutive Kolmogorov-Arnold networks (CKANs): combining accuracy and interpretability in data-driven material modeling. https://doi.org/10.48550/arXiv.2502.05682

Abdusalamov, R., Hillgärtner, M., Itskov, M., et al., 2023. Automatic generation of interpretable hyperelastic material models by symbolic regression. Int. J. Numer. Methods Eng. , nme.7203 https://doi.org/10.1002/nme.7203

Anssari-Benam, A., 2023. Large isotropic elastic deformations: on a comprehensive model to correlate the theory and experiments for incompressible rubber-like materials. J. Elast. 153 (2), 219–244. https://doi.org/10.1007/s10659-022-09982-5

Anssari-Benam, A., Destrade, M., Saccomandi, G., 2022. Modelling brain tissue elasticity with the Ogden model and an alternative family of constitutive models†. Philos. Trans. R. Soc. A: Math. Phys. Eng. Sci. 380 (2234), 20210325. https://doi.org/10.1098/rsta.2021.0325

Anton, D., Wessels, H., 2022. Physics-informed neural networks for material model calibration from full-field displacement data. http://arxiv.org/abs/2212.07723.

Avril, S., Bonnet, M., Bretelle, A.-S., Grédiac, M., Hild, F., Ienny, P., Latourte, F., Lemosse, D., Pagano, S., Pagnacco, E., Pierron, F., et al., 2008. Overview of identification methods of mechanical parameters based on full-field measurements. Exp. Mech. 48 (4), 381–402. https://doi.org/10.1007/s11340-008-9148-y

Blatz, P.J., Ko, W.L., 1962. Application of finite elastic theory to the deformation of rubbery materials. Trans. Soc. Rheol. 6 (1), 223–252. https://doi.org/10.1122/1.548937

Boes, B., Simon, J.-W., Holthusen, H., et al., 2024. Accounting for plasticity: an extension of inelastic constitutive artificial neural networks. http://arxiv.org/abs/2407.19326.

Boyce, M., Arruda, E., 2000. Constitutive models of rubber elasticity: a review. Rubber Chem. Technol. 73, 504–523. https://doi.org/10.5254/1.3547602

Budday, S., Sommer, G., Birkl, C., Langkammer, C., Haybaeck, J., Kohnert, J., Bauer, M., Paulsen, F., Steinmann, P., Kuhl, E., Holzapfel, G.A., et al., 2017. Mechanical characterization of human brain tissue. Acta Biomater. 48, 319–340. https://doi.org/10.1016/j.actbio.2016.10.036

Dammaß, F., Kalina, K.A., Kästner, M., 2025. When invariants matter: the role of I1 and I2 in neural network models of incompressible hyperelasticity. Mech. Mater., 105443. https://doi.org/10.1016/j.mechmat.2025.105443

Demiray, H., 1972. A note on the elasticity of soft biological tissues. J. Biomech. 5 (3), 309–311. https://doi.org/10.1016/0021-9290(72)90047-4

Efron, B., Hastie, T., Johnstone, I., Tibshirani, R., et al., 2004. Least angle regression. Ann. Stat. 32 (2), 407–499.

Flaschel, M., Hastie, T., Kuhl, E., et al., 2025a. Non-smooth optimization meets automated material model discovery. https://doi.org/10.48550/arXiv.2507.10196

Flaschel, M., Kumar, S., De Lorenzis, L., et al., 2021. Unsupervised discovery of interpretable hyperelastic constitutive laws. Comput. Methods Appl. Mech. Eng. 381, 113852. https://doi.org/10.1016/j.cma.2021.113852

Flaschel, M., Martonová, D., Veil, C., Kuhl, E., et al., 2025b. Material fingerprinting: a shortcut to material model discovery without solving optimization problems. https://doi.org/10.48550/arXiv.2508.07831

Flaschel, M., Martonová, D., Veil, C., Kuhl, E., 2025c. Python package for Material Fingerprinting. Zenodo. https://doi.org/10.5281/zenodo.17098250

Flaschel, M., Yu, H., Reiter, N., Hinrichsen, J., Budday, S., Steinmann, P., Kumar, S., De Lorenzis, L., et al., 2023. Automated discovery of interpretable hyperelastic material models for human brain tissue with EUCLID. J. Mech. Phys. Solids 180, 105404. https://doi.org/10.1016/j.jmps.2023.105404

Frank, I.E., Friedman, J.H., 1993. A statistical view of some chemometrics regression tools. Technometrics 35 (2), 109–135. https://doi.org/10.1080/00401706.1993.10485033

Fuhg, J.N., Anantha Padmanabha, G., Bouklas, N., Bahmani, B., Sun, W., Vlassis, N.N., Flaschel, M., Carrara, P., De Lorenzis, L., et al., 2024. A review on data-driven constitutive laws for solids. Arch. Comput. Methods Eng. https://doi.org/10.1007/s11831-024-10196-2

Gent, A.N., Thomas, A.G., 1958. Forms for the stored (strain) energy function for vulcanized rubber. J. Polym. Sci. 28 (118), 625–628. https://doi.org/10.1002/pol.1958.1202811814

Ghaboussi, J., Garrett, J.H., Wu, X., et al., 1991. Knowledge-based modeling of material behavior with neural networks. J. Eng. Mech. 117 (1), 132–153. https://doi.org/10.1061/(ASCE)0733-9399(1991)117:1(132)

Ghouli, S., Flaschel, M., Kumar, S., De Lorenzis, L., et al., 2025. A topology optimisation framework to design test specimens for one-shot identification or discovery of material models. J. Mech. Phys. Solids 203, 106210. Publisher: Elsevier BV. https://doi.org/10.1016/j.jmps.2025.106210

Grédiac, M., 1989. Principle of virtual work and identification. Compt. Rendus de L Acad. Sci. Ser. Ii (309(1)), 1–5.

Guan, D., Ahmad, F., Theobald, P., Soe, S., Luo, X., Gao, H., et al., 2019. On the AIC-based model reduction for the general Holzapfel–ogden myocardial constitutive law. Biomech. Model. Mechanobiol. 18 (4), 1213–1232. https://doi.org/10.1007/s10237-019-01140-6

Hartmann, S., 2001. Parameter estimation of hyperelasticity relations of generalized polynomial-type with constraint conditions. Int. J. Solids Struct. 38 (44–45), 7999–8018. https://doi.org/10.1016/S0020-7683(01)00018-X

Holzapfel, G.A., Gasser, T.C., Ogden, R.W., et al., 2004. A new constitutive framework for arterial wall mechanics and a comparative study of material models. In: Cowin, S.C., Humphrey, J.D. (Eds.), Cardiovascular Soft Tissue Mechanics. Kluwer Academic Publishers, Dordrecht, pp. 1–48. https://doi.org/10.1007/0-306-48389-0_1

Ibañez, R., Abisset-Chavanne, E., Aguado, J.V., Gonzalez, D., Cueto, E., Chinesta, F., et al., 2018. A manifold learning approach to data-driven computational elasticity and inelasticity. Arch. Comput. Methods Eng. 25 (1), 47–57. https://doi.org/10.1007/s11831-016-9197-9

Kirchdoerfer, T., Ortiz, M., 2016. Data-driven computational mechanics. Comput. Methods Appl. Mech. Eng. 304, 81–101. https://doi.org/10.1016/j.cma.2016.02.001

Kissas, G., Mishra, S., Chatzi, E., De Lorenzis, L., et al., 2024. The language of hyperelastic materials. Comput. Methods Appl. Mech. Eng. 428, 117053. https://doi.org/10.1016/j.cma.2024.117053

Klein, D.K., Fernández, M., Martin, R.J., Neff, P., Weeger, O., et al., 2022. Polyconvex anisotropic hyperelasticity with neural networks. J. Mech. Phys. Solids 159, 104703. https://doi.org/10.1016/j.jmps.2021.104703

Lemaitre, J., Chaboche, J.-L., 1994. Mechanics of Solid Materials. Cambridge university press.

Linka, K., Kuhl, E., 2023. A new family of constitutive artificial neural networks towards automated model discovery. Comput. Methods Appl. Mech. Eng. 403, 115731. https://doi.org/10.1016/j.cma.2022.115731

Linka, K., Sarah, R.S.P., Kuhl, E., et al., 2023. Automated model discovery for human brain using constitutive artificial neural networks. Acta Biomater. 160, 134–151. https://doi.org/10.1016/j.actbio.2023.01.055

Ma, D., Gulani, V., Seiberlich, N., Liu, K., Sunshine, J.L., Duerk, J.L., Griswold, M.A., et al., 2013. Magnetic resonance fingerprinting. Nature 495 (7440), 187–192. https://doi.org/10.1038/nature11971

Martonová, D., Goriely, A., Kuhl, E., et al., 2025. Generalized invariants meet constitutive neural networks: A novel framework for hyperelastic materials. J. Mech. Phys. Solids 206, 106352. https://doi.org/10.1016/j.jmps.2025.106352

Martonová, D., Peirlinck, M., Linka, K., Holzapfel, G.A., Leyendecker, S., Kuhl, E., et al., 2024. Automated model discovery for human cardiac tissue: discovering the best model and parameters. Comput. Methods Appl. Mech. Eng. 428, 117078. https://doi.org/10.1016/j.cma.2024.117078

Martonová, D., Leyendecker, S., Holzapfel, G.A., Kuhl, E., et al., 2025. Discovering dispersion: how robust is automated model discovery for human myocardial tissue?. Biomech. Model. Mechanobiol. 24, 2023–2037. https://doi.org/10.1007/s10237-025-02005-x

Masi, F., Stefanou, I., Vannucci, P., Maffi-Berthier, V., et al., 2021. Thermodynamics-based artificial neural networks for constitutive modeling. J. Mech. Phys. Solids 147, 104277. https://doi.org/10.1016/j.jmps.2020.104277

McGivney, D.F., Pierre, E., Ma, D., Jiang, Y., Saybasili, H., Gulani, V., Griswold, M.A., et al., 2014. SVD Compression for magnetic resonance fingerprinting in the time domain. IEEE Trans. Med. Imaging 33 (12), 2311–2322. https://doi.org/10.1109/TMI.2014.2337321

Mihai, L.A., Budday, S., Holzapfel, G.A., Kuhl, E., Goriely, A., 2017. A family of hyperelastic models for human brain tissue. J. Mech. Phys. Solids 106, 60–79. https://doi.org/10.1016/j.jmps.2017.05.015

Mihai, L.A., Chin, L., Janmey, P.A., Goriely, A., 2015a. A comparison of hyperelastic constitutive models applicable to brain and fat tissues. J. R. Soc. Interface 12 (110), 20150486. https://doi.org/10.1098/rsif.2015.0486

Mihai, L.A., Chin, L., Janmey, P.A., Goriely, A., et al., 2015b. A comparison of hyperelastic constitutive models applicable to brain and fat tissues. J. R. Soc. Interface 12 (110), 20150486. https://doi.org/10.1098/rsif.2015.0486

Miller, K., Chinzei, K., Orssengo, G., Bednarz, P., 2000. Mechanical properties of brain tissue in-vivo: experiment and computer simulation. J. Biomech. 33 (11), 1369–1376. https://doi.org/10.1016/S0021-9290(00)00120-2

Moreno-Mateos, M.A., Wiesheier, S., Esmaeili, A., Hossain, M., Steinmann, P., et al., 2025. Biaxial characterization of soft elastomers: experiments and data-adaptive configurational forces for fracture. J. Mech. Phys. Solids 205, 106339. https://doi.org/10.1016/j.jmps.2025.106339

Mozaffar, M., Bostanabad, R., Chen, W., Ehmann, K., Cao, J., Bessa, M.A., et al., 2019. Deep learning predicts path-dependent plasticity. Proc. Nat. Acad. Sci. 116 (52), 26414–26420. https://doi.org/10.1073/pnas.1911815116

Ogden, R.W., 1972. Large deformation isotropic elasticity – on the correlation of theory and experiment for incompressible rubberlike solids. Proc. R. Soc. London. Series A Math. Phys. Sci. 326 (1567), 565–584.

Ogden, R.W., 1997. Non-Linear Elastic Deformations. Courier Corporation.

Pierron, F., Grédiac, M., 2012. The Virtual Fields Method. Springer New York, New York, NY. https://doi.org/10.1007/978-1-4614-1824-5

Pierron, F., Grédiac, M., 2020. Towards material testing 2.0. a review of test design for identification of constitutive parameters from full-field measurements. Strain https://doi.org/10.1111/str.12370

Rivlin, 1950. Large elastic deformations of isotropic materials. I. fundamental concepts, 241 (835), 32.

Rosenkranz, M., Kalina, K.A., Brummund, J., Kästner, M., et al., 2023. A comparative study on different neural network architectures to model inelasticity. Int. J. Numer. Methods Eng. 124 (21), 4802–4840. https://doi.org/10.1002/nme.7319

Roux, S., Hild, F., 2020. Optimal procedure for the identification of constitutive parameters from experimentally measured displacement fields. Int. J. Solids Struct. 184, 14–23. https://doi.org/10.1016/j.ijsolstr.2018.11.008

Rouze, N.C., Deng, Y., Trutna, C.A., Palmeri, M.L., Nightingale, K.R., et al., 2018. Characterization of viscoelastic materials using group shear wave speeds. IEEE Trans. Ultrason. Ferroelectr. Freq. Contr. 65 (5), 780–794. https://doi.org/10.1109/TUFFC.2018.2815505

Römer, U., Hartmann, S., Tröger, J.-A., Anton, D., Wessels, H., Flaschel, M., De Lorenzis, L., et al., 2025. Reduced and all-at-once approaches for model calibration and discovery in computational solid mechanics. Appl. Mech. Rev. 77 (4), 040801. https://doi.org/10.1115/1.4066118

Sarah, R.S.P., Linka, K., Kuhl, E., et al., 2023. Principal-stretch-based constitutive neural networks autonomously discover a subclass of Ogden models for human brain tissue. Brain Multiphys. 4, 100066. https://doi.org/10.1016/j.brain.2023.100066

Schoenauer, M., Sebag, M., Jouve, F., Lamy, B., Maitournam, H., et al., 1996. Evolutionary identification of macro-mechanical models. Adv. Genet. Prog. II, 467–488.

Shojaee, M., Rezaei, S., Weeger, O., et al., 2025. Automated discovery of effective material models for nonhomogeneous hyperelastic materials. https://doi.org/10.21203/rs.3.rs-6963603/v1

Thakolkaran, P., Guo, Y., Saini, S., Peirlinck, M., Alheit, B., Kumar, S., et al., 2025. Can KAN CANs? Input-convex Kolmogorov-Arnold networks (KANs) as hyperelastic constitutive artificial neural networks (CANs). https://doi.org/10.48550/arXiv.2503.05617

Tibshirani, R., 1996. Regression Shrinkage and selection via the Lasso. J. R. Stat. Soc. Series B (Methodol.) 58 (1), 267–288. https://doi.org/10.1111/j.2517-6161.1996.tb02080.x

Treloar, L.R.G., 1944. Stress-strain data for vulcanised rubber under various types of deformation. Trans. Faraday Soc. 40, 59. https://doi.org/10.1039/tf9444000059

Trutna, C.A., Knight, A.E., Rouze, N.C., Hobson-Webb, L.D., Palmeri, M.L., Nightingale, K.R., et al., 2020a. Viscoelastic characterization in muscle using group speed analysis and volumetric shear wave elasticity imaging. In: 2020 IEEE International Ultrasonics Symposium (IUS). IEEE, Las Vegas, NV, USA, pp. 1–4. https://doi.org/10.1109/IUS46767.2020.9251751

Trutna, C.A., Rouze, N.C., Palmeri, M.L., Nightingale, K.R., et al., 2019. Robust model-based viscoelastic characterization of QIBA phantoms through fractional derivative group shear wave speeds. In: 2019 IEEE International Ultrasonics Symposium (IUS). IEEE, Glasgow, United Kingdom, pp. 1391–1394. https://doi.org/10.1109/ULTSYM.2019.8925625

Trutna, C.A., Rouze, N.C., Palmeri, M.L., Nightingale, K.R., et al., 2020b. Measurement of viscoelastic material model parameters using fractional derivative group shear wave speeds in simulation and phantom data. IEEE Trans. Ultrason. Ferroelectr. Freq. Contr. 67 (2), 286–295. https://doi.org/10.1109/TUFFC.2019.2944126

Versino, D., Tonda, A., Bronkhorst, C.A., et al., 2017. Data driven modeling of plastic deformation. Comput. Methods Appl. Mech. Eng. 318, 981–1004. https://doi.org/10.1016/j.cma.2017.02.016

Wang, M., Chen, C., Liu, W., 2022. Establish algebraic data-driven constitutive models for elastic solids with a tensorial sparse symbolic regression method and a hybrid feature selection technique. J. Mech. Phys. Solids 159, 104742.

Wang, Z., Estrada, J.B., Arruda, E.M., Garikipati, K., et al., 2021. Inference of deformation mechanisms and constitutive response of soft material surrogates of biological tissue by full-field characterization and data-driven variational system identification. J. Mech. Phys. Solids 153, 104474. https://doi.org/10.1016/j.jmps.2021.104474

Wiesheier, S., Moreno-Mateos, M.A., Steinmann, P., et al., 2024. Versatile data-adaptive hyperelastic energy functions for soft materials. Comput. Methods Appl. Mech. Eng. 430, 117208. https://doi.org/10.1016/j.cma.2024.117208

Wittwer, L.D., Reichel, F., Müller, P., Guck, J., Aland, S., et al., 2023. A new hyperelastic lookup table for RT-DC. Soft Matter. 19 (11), 2064–2073. https://doi.org/10.1039/D2SM01418A

Xu, H., Flaschel, M., De Lorenzis, L., et al., 2025. Discovering non-associated pressure-sensitive plasticity models with EUCLID. Adv. Model. Simul. Eng. Sci. 12 (1), 1. https://doi.org/10.1186/s40323-024-00281-3

Yohsuke, B., Urayama, K., Takigawa, T., Ito, K., 2011. Biaxial strain testing of extremely soft polymer gels. Soft Matter. 7 (6), 2632. https://doi.org/10.1039/c0sm00955e